GSI 2021, July 21st 2021

The primary visual cortex as a Cartan engine

Jean Petitot,
CAMS, EHESS, Paris,
jean.petitot@ehess.fr

1. Introduction

Cortical visual neurons detect very *local* geometric cues at retinal positions (local contrasts, local orientations of boundaries, curvatures, crossings, cusps, etc.). One of the main theoretical problem of low level vision is to understand how these local cues can be *integrated* so as to generate the *global* geometry of the images perceived, with all the well-known phenomena studied since Gestalt theory.

It is an empirical evidence that the visual brain is able to perform a lot of differential routines. But how such routines can be *neurally* implemented? At their resolution scale, neurons are "point-like" processors and it seems impossible to compute differential routines with them.

2. Introduction

Since the 1990s, revolutionary methods of "in vivo optical imaging" enabled to visualize the extremely special connectivity of the primary visual areas, that is their "functional architectures".

What we called "Neurogeometry" is based on the discovery that these *hardwired* and *modular* functional architectures implement structures such as the contact structure and the sub-Riemannian geometry of jet spaces of plane curves.

For principled reasons, it is the geometrical reformulation of differential calculus from Pfaff to Lie, Darboux, Frobenius, Cartan and Goursat which turns out to be suitable for neurogeometry.

3. Images of H&W

The story begins with the breakthrough recordings of V1 neurons in the early 60s by David Hubel and Torsten Wiesel (Nobel prizes in 1981).

These neurons detect a *preferred orientation p* crossing their receptive field centered on a retinal position *a*. When they are activated they fire and emit spikes and the spikes can be recorded using electrodes.

This is one of the breakthrough images of the history of science, analogous to the first observation and identification of the rings of Saturn by Galileo (1610) then Huygens (1655) using an astronomical telescope, or the first observation of biological cells by Hooke (1665) using a microscope.

4. H&W breakthrough

Here are two images of a 40s recording.
Left: a bar aligned along the preferred orientation (noisy firing).
Right: a bar orthogonal to the preferred orientation (quiet, no firing)

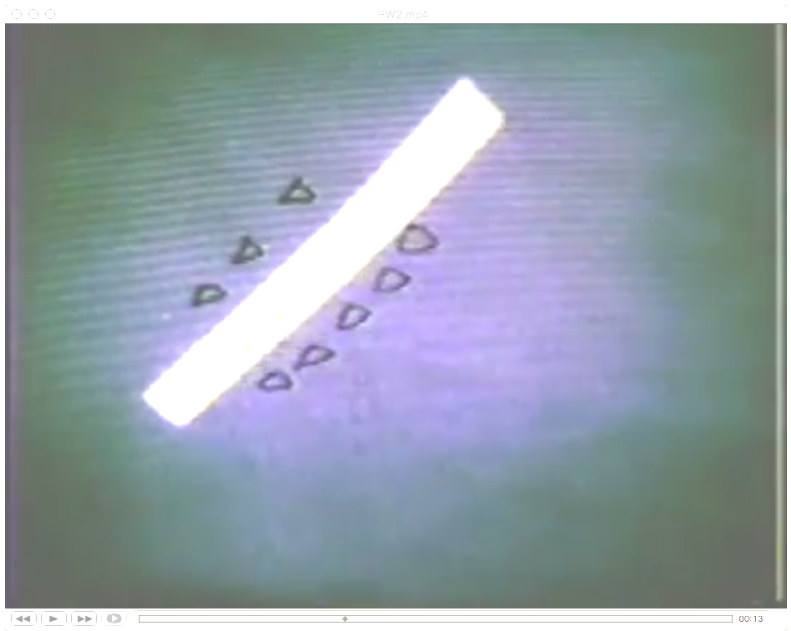

Moreover, Hubel and Wiesel discovered that

Neurons detecting all the orientations p at the same retinal position $a \in \mathbb{R}^2$ constitute an anatomically well delimited small neural module called an "orientation hypercolumn".

and that preferred orientations p vary smoothly with the retinal point a. So the (a, p) constitute an *orientation field*.

6. Braitenberg abduction

The first global reconstruction of an orientation field from the sparse local data provided by electrodes was *infered* abductively in 1979 by Valentino and Carla Braitenberg.

This was long before the introduction of modern *in vivo* optical imaging techniques.

They claimed:

> *"We believe that the most natural explanation of the facts observed would be in terms of orientations arranged with circular symmetry around centers, either radially or along concentric circles."*

7. Swindale's abduction

After Braitenberg, in an astonishing 1987 paper (still before the advent of optical imaging techniques), Nicholas Swindale reconstructed (for the cat's area 18), the "spatial layout" of the orientation map.

He thus confirmed Braitenberg's abduction.

His data came from electrodes separated by about $150 - 300\mu m$ at a cortical depth of about $400 - 700\mu m$.

He succeeded in *interpolating* between the prefered orientations measured at the different sites and reconstructed the "fine grained" map shown in the following figure.

It was a great achievement.

8. Swindale's image 1

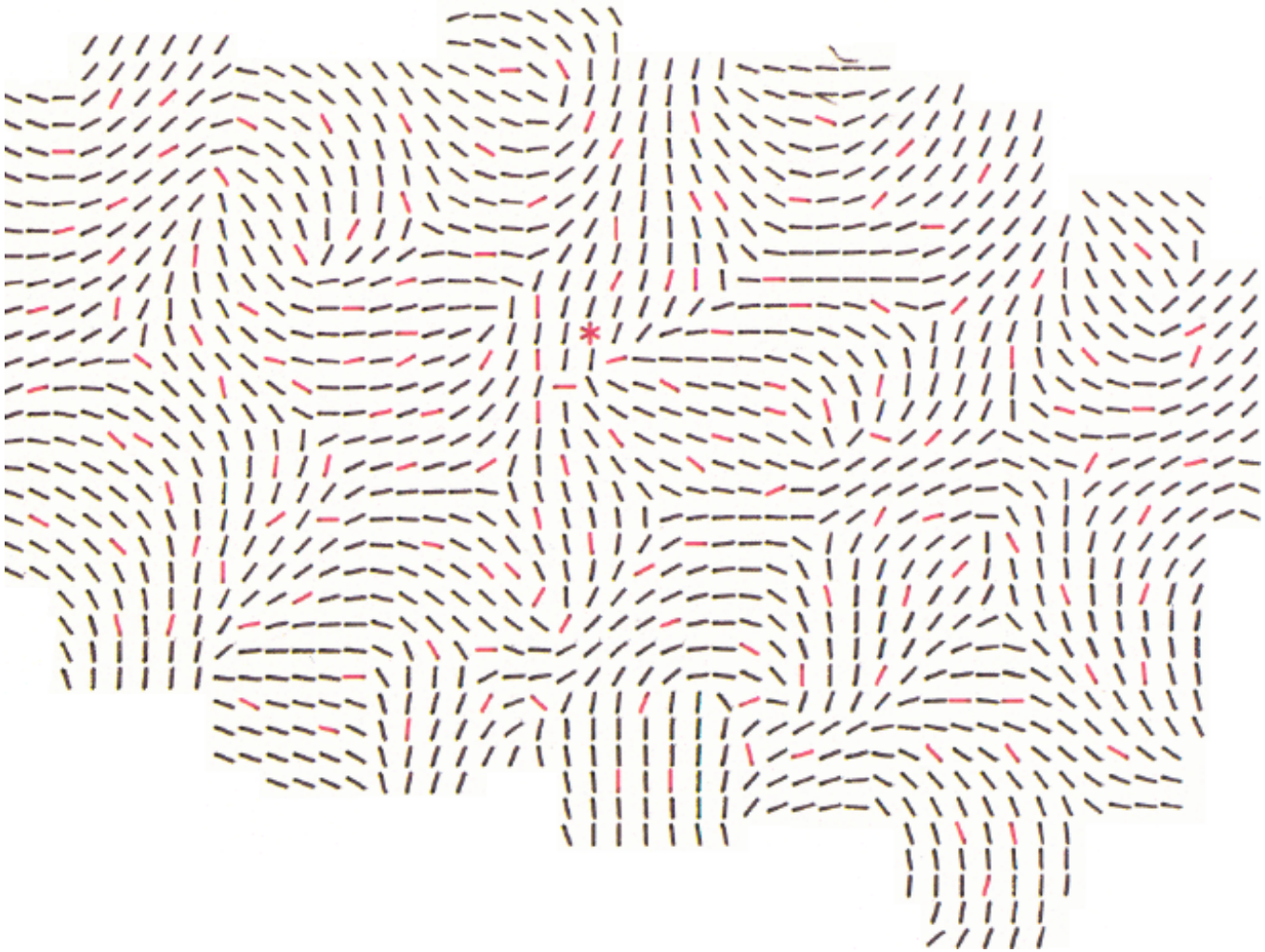

9. Swindale's image 2

Using a color code for directions, he got an orientation map.

This is a theoretical reconstruction and not an empirical observation.

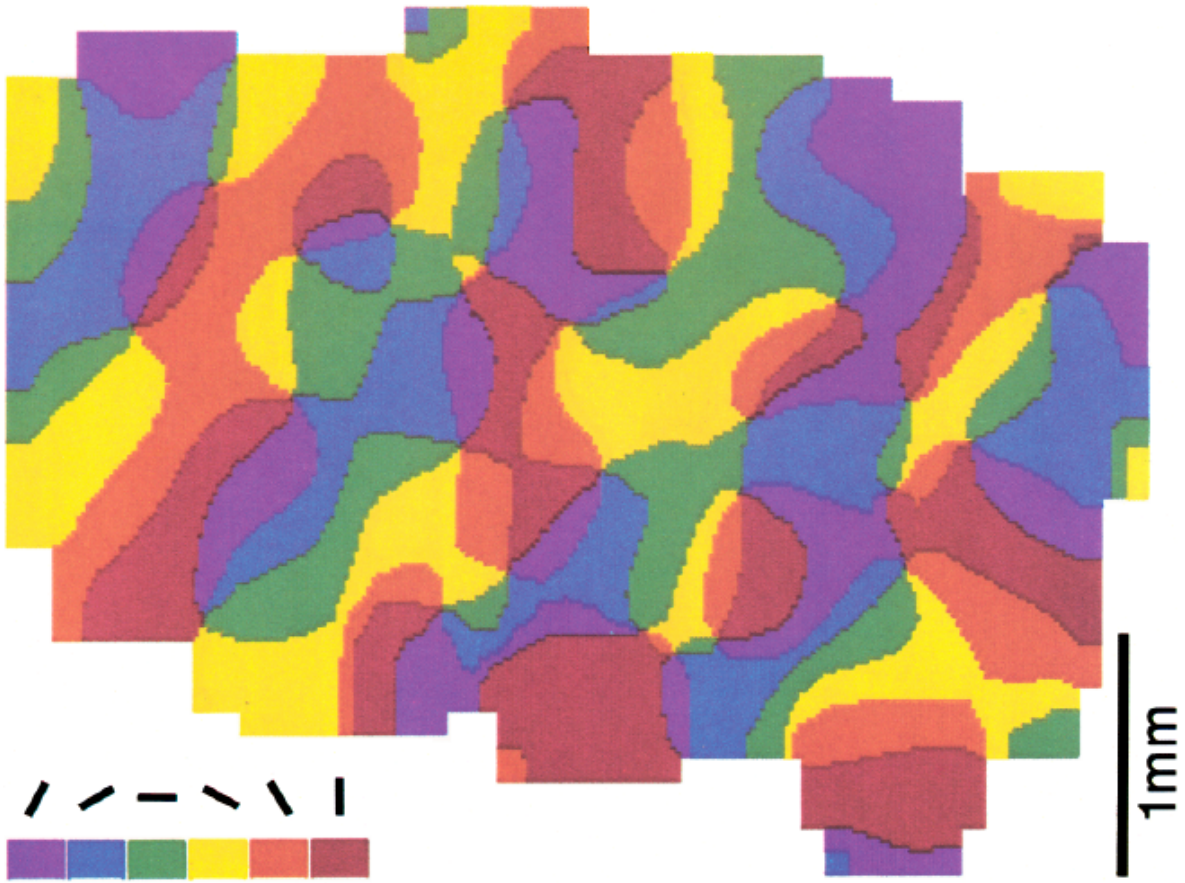

10. Swindale's image 3

He even reconstructed the possible *singularities* of the orientation field: they can be end points or triple points.

What are now called *pinwheels*.

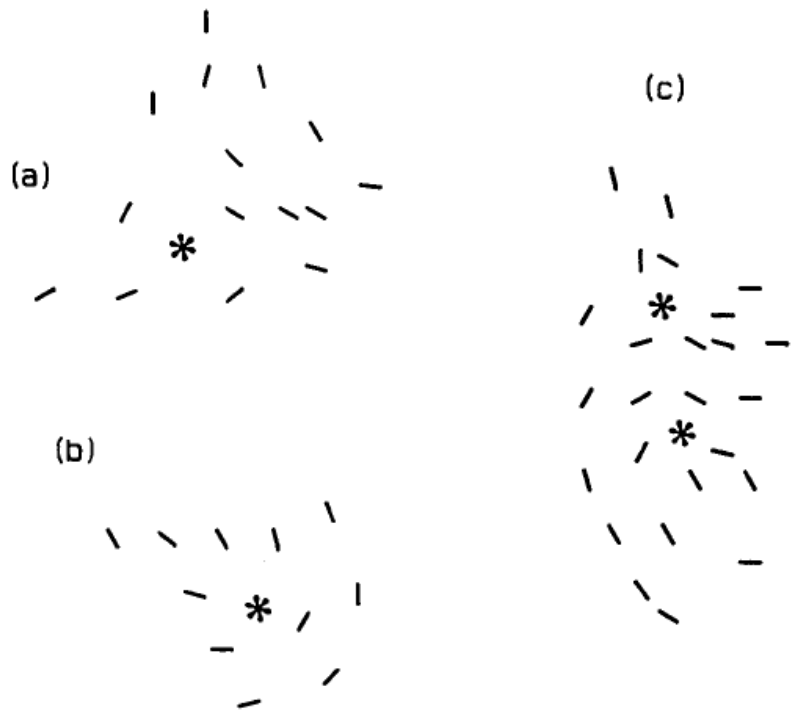

11. In vivo optical imaging

Braitenberg's and Swindale's abductions have been strikingly confirmed in the 1990s by brain imagery and techniques of "in vivo optical imaging based on activity-dependent intrinsic signals" (Amiram Grinvald and Tobias Bonhöffer).

They used the fact that the metabolic activity of cortical layers change their optical properties (differential absorption of oxyhemoglobin or deoxyhemoglobin whose fluorescence is an index of the local depolarisation of neurons).

This enables to acquire *in vivo* images of the activity of the superficial cortical layers.

12. In vivo optical imaging II

As Kenichi Ohki and Clay Reid have pointed out,

> *"optical imaging revolutionized the study of functional architecture by showing the overall geometry of functional maps."*

The scale of observation is a "meso"-scale.

For a true "micro"-scale observation at the level of single neurons, you need more recent techniques such as "two-photon confocal microscopy" (Kenichi Ohki 2006).

13. Orientation maps

Here is the functional architecture of the area $V1$ of a tree-shrew (tupaya) obtained by in vivo optical imaging (William Bosking with David Fitzpatrick's team at Duke University).

They used "grattings", that is large grids of parallel dark stripes translated in the visual field.

For every orientation (coded by the bottom-right color) they got a global map of activity (dark = active).

This is now an empirical observation and not a theoretical reconstruction.

14. Orientation maps. Image

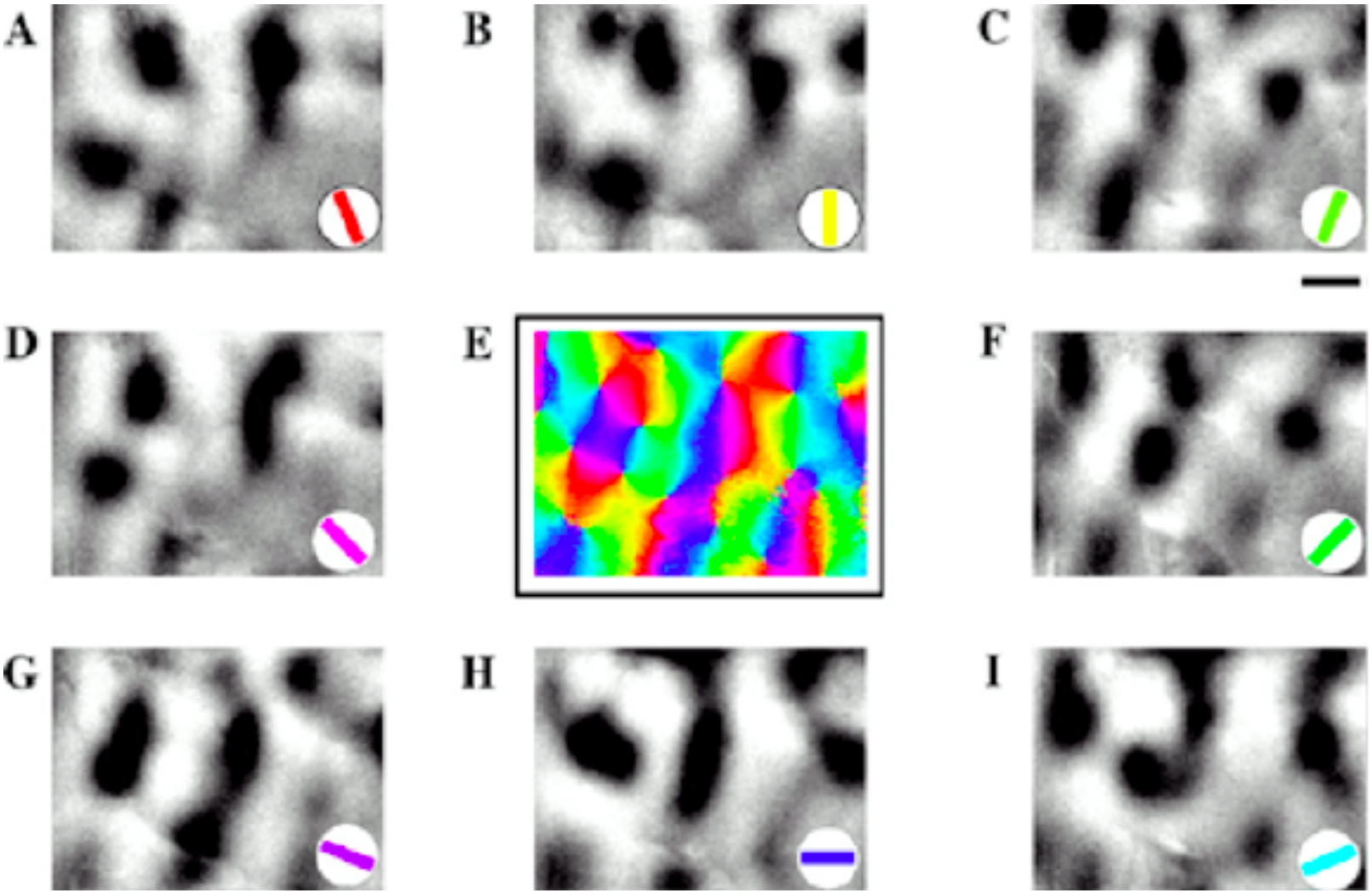

15. Pinwheels

Orientation maps with pinwheels are now well known. Here is the $V1$ area of the macaque by Blasdel and Salama,

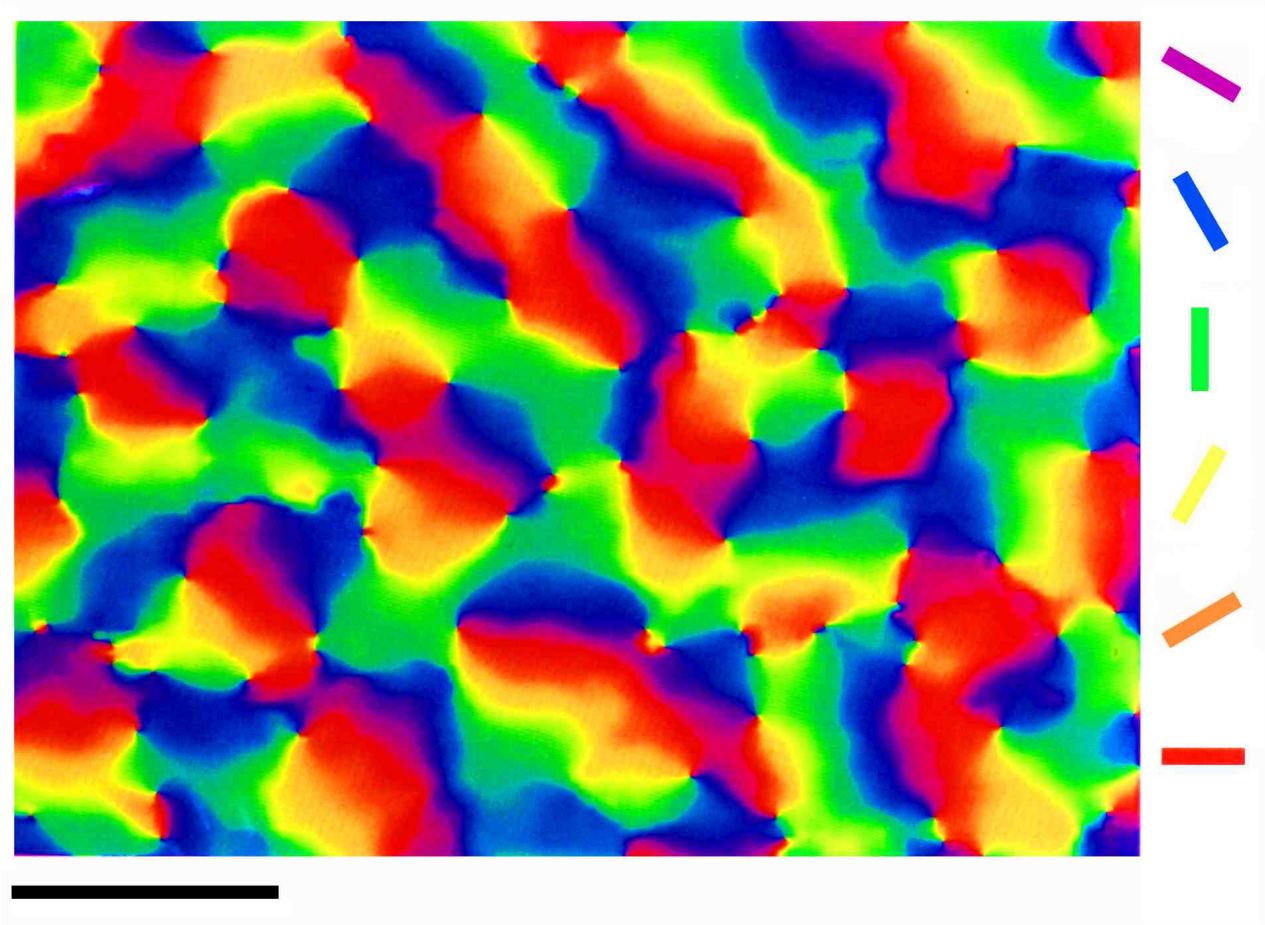

16. End points and triple points

In the following picture due to Shmuel (cat's area 17), orientations are coded by colors but are also represented by small white segments.

We observe very well the two types of generic singularities of 1D foliations in the plane anticipated by Braitenberg and Swindale.

17. Shmuel's orientation map

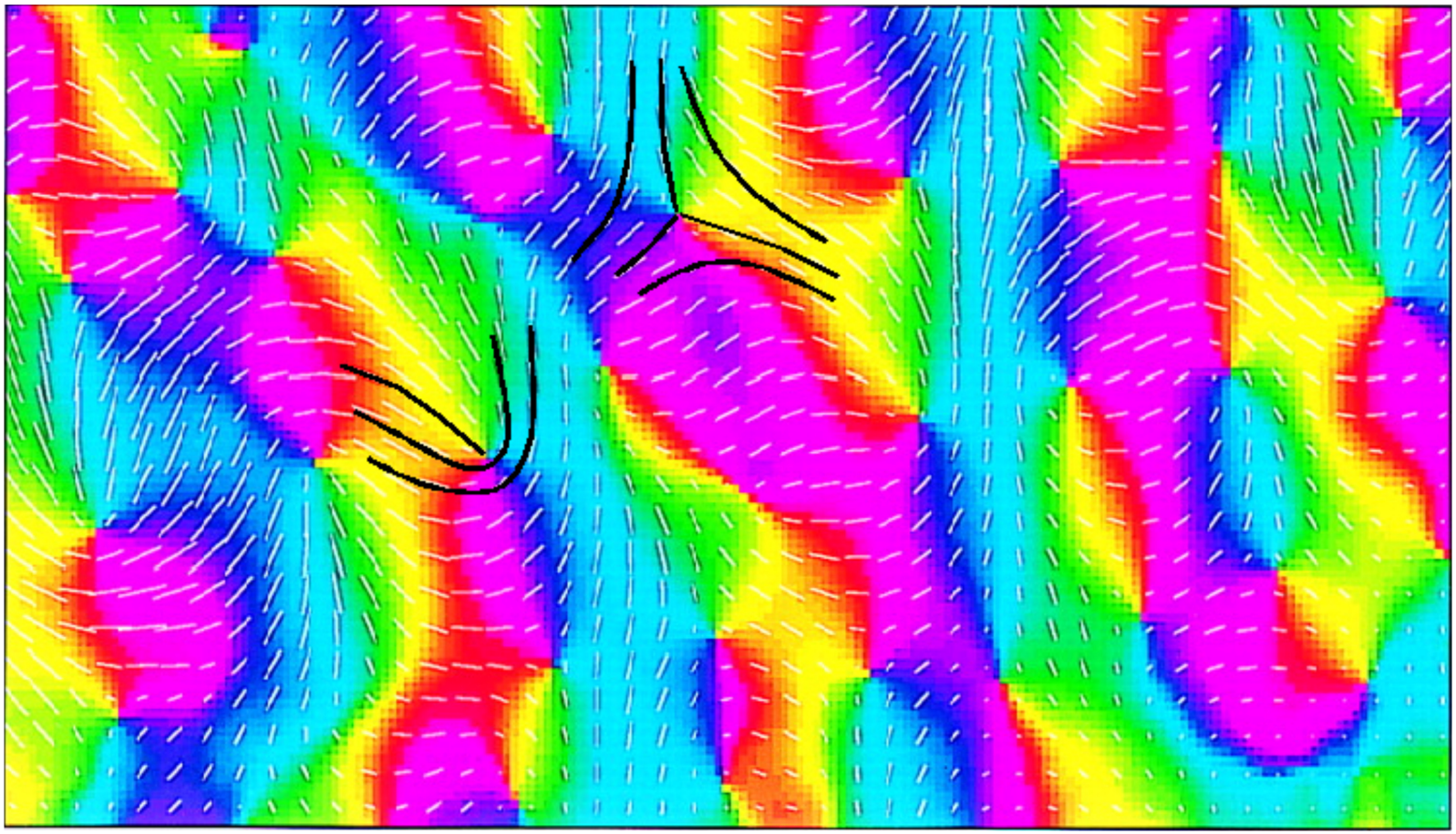

18. Pinwheels' structure

- The plane is $V1$,
- A colored point represents the mean of a small group of real neurons (meso-scale).
- Colors code for the preferred orientation at each point.
- The field of isochromatic lines (i.e. iso-orientation lines) is organized by a lattice of *singular points* (pinwheels) where all orientations meet (distant about 1200μm in cats and about 600μm in primates).
- There exists a "mesh" of the lattice of pinwheels (a sort of characteristic length).
- Pinwheels have a chirality.
- Adjacent pinwheels have opposed chirality.

19. Pinwheels (*bis repetita*)

Left: local triviality. Right: two pinwheels of opposed chiralities.

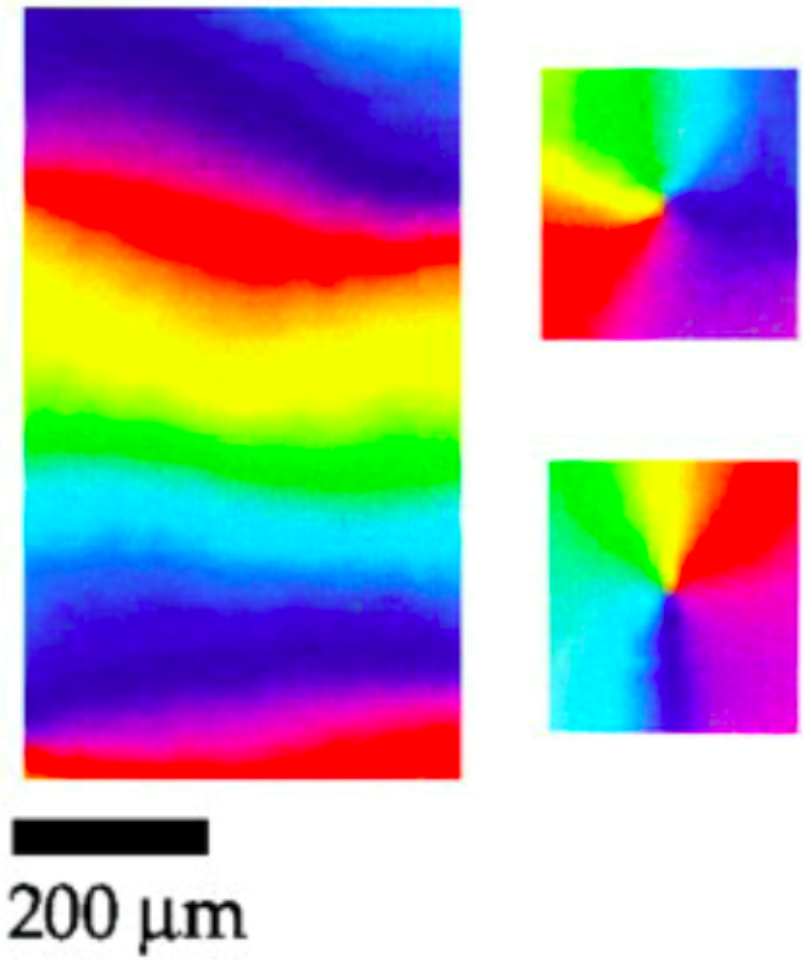

20. Interspecific functional architecture

A pinwheel organisation can be found in many species: cat, primate (marmoset), tupaya (tree shrew), prosimian Bush Baby, tawny owl, etc.

It is a widely interspecific functional architecture.

The following figure shows pinwheels in the $V1$ and $V2$ areas of the cat, (A) and (B), the marmoset (C) and (D), and the tawny owl (E) and (F).

21. Pinwheels in different species

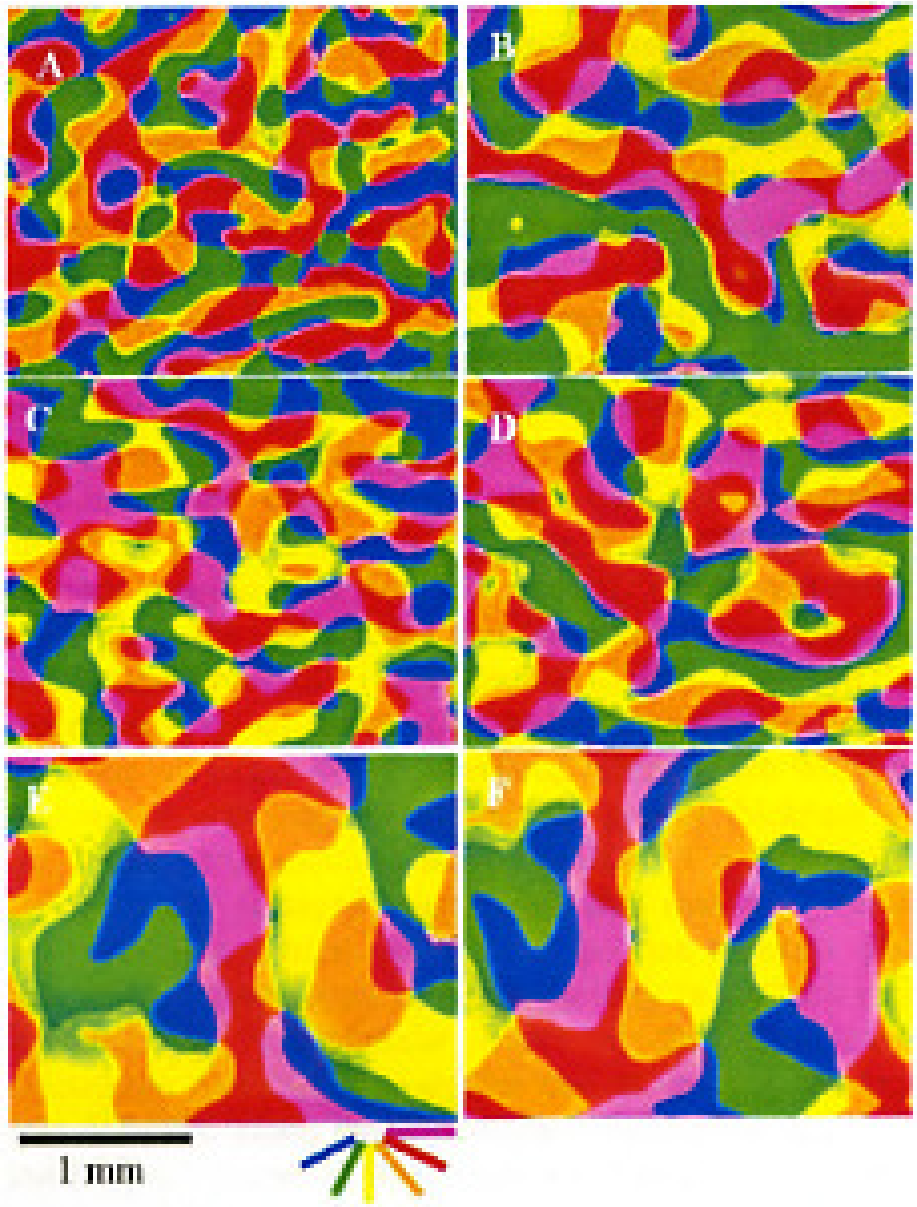

22. Periodicity of pinwheels

Orientation maps (image A: left) are as *phase fields* in optics. They manifest a *periodicity*. The *power spectrum* (the Fourier transform of the autocorrelation function of the map) is concentrated on a *ring* of average radius $k_0 = \frac{2\pi}{\Lambda_0}$ (image B: right)

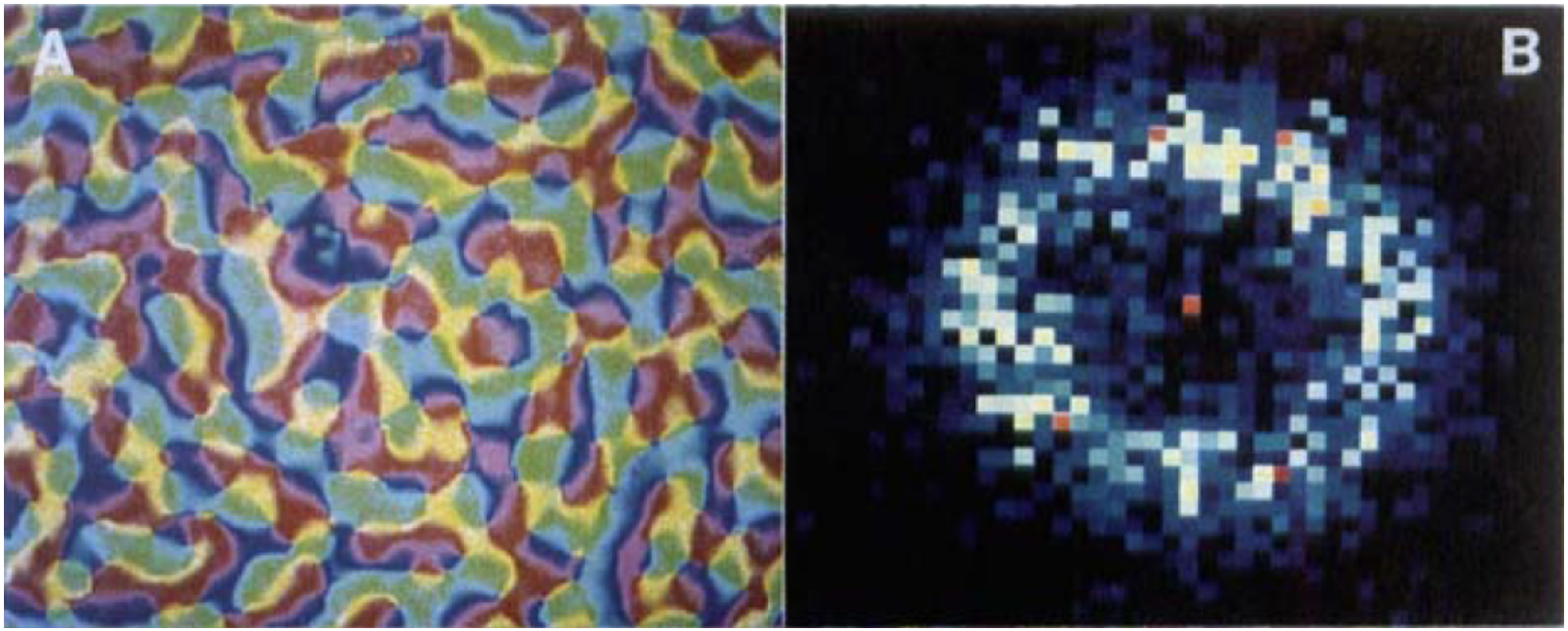

23. Superposition of plane waves

This means that, ideally, such phase fields with a characteristic length are superpositions of plane waves with random phases but sharing *the same* wave number k

The following figure shows pinwheels in a superposition of 10 plane waves with the same wave number $k = 1$ and random phases φ. (The white cuts represent $\varphi = 0 = 2\pi$).

24. Pinwheels in superpositions of plane waves

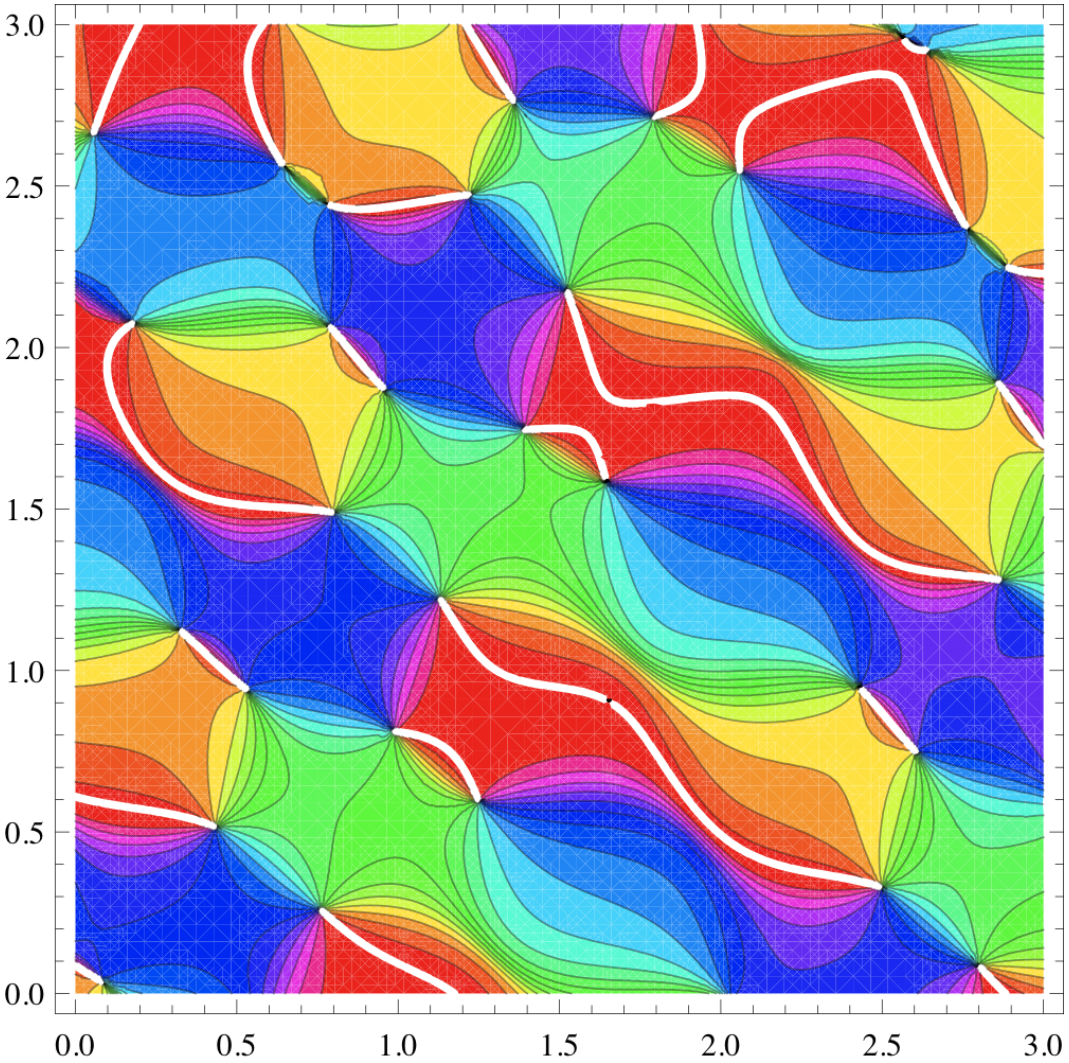

25. Statistics of pinwheels and Gaussian fields

The statistics of singularities of phase fields is a beautiful subject. Under some simplifying hypotheses, they can be modeled by *Gaussian random fields* (see works of Fred Wolf and Theo Geisel, Michael Berry and Mark Dennis, Robert Adler and Jonathan Taylor, and also Daniel Bennequin and Alexandre Afgoustidis, Giovanna Citti, Alessandro Sarti and Davide Barbieri).

In that case, you can prove that the *density of singularities* is $d = \frac{k^2}{4\pi} = \frac{\pi}{\Lambda^2}$ with $\Lambda = \frac{2\pi}{k}$.

It is remarkable that this density $\frac{\pi}{\Lambda^2}$ was also found *empirically* in pinwheels map.

26. Pinwheels as blowing-up

Pinwheels can be interpreted geometrically as *blowing-up* of points a_i and the orientation field is the closure of a section σ of the fiber bundle $\pi : \mathbb{V}_J = \mathbb{R}^2 \times \mathbb{P}^1 \to \mathbb{R}^2$ (J for "jets") defined over the open subset $\mathbb{R}^2 - \{a_i\}$.

Over the a_i the closure of σ is the "exceptionnal" fiber $\mathbb{P}^1_{a_i}$.

These exceptional fibers $\mathbb{P}^1_{a_i}$ are "contracted" and "folded" onto small wheels around the base points a_i.

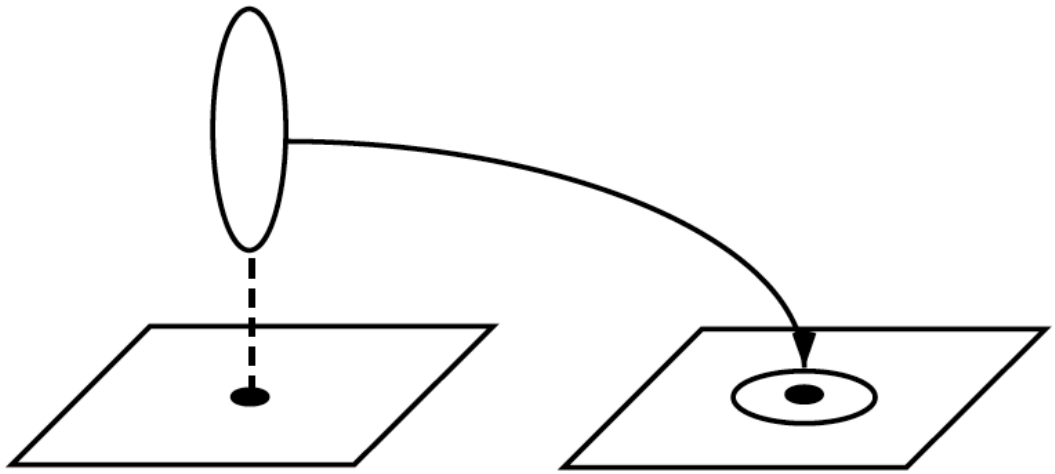

27. V1 as fiber bundle

There is therefore a $3D \longrightarrow 2D$ dimensional collapse : an orientation map is, in a way, a geometric object of "intermediate" dimension between 2 and 3, with a lattice of base points blown-up in parallel,

At the limit, when all the points of the base plane $\mathbb{R}^2$ are blown-up in parallel, we get the fiber bundle $\pi : \mathbb{V}_J = \mathbb{R}^2 \times \mathbb{P}^1 \longrightarrow \mathbb{R}^2$.

So $\mathbb{V}_J$ can be considered as an *idealized continuous model* of the concrete neural $V1$ produced by biological evolution with its lattice of pinwheels and orientation field.

28. Receptive fields and receptive profiles

Let me add some further remarks on low level cortical visual neurons.

A first remark is that, at a very rough linear approximation, they act as *filters* on the optical signal transduced by the photoreceptors.

They are connected to a small domain D of the photoreceptor layer, called their *receptive field* and their transfer function as filter is called their *receptive profile*.

The shape of the receptive profile determines the geometric cue preferrentially detected by the neuron.

29. Receptive profiles as Gaussian derivatives

The receptive profiles are well modeled either by derivatives of Gaussian G or by Gabor patches.

The width σ of G defines a *scale* and the neuron is a *point-like processor* at this scale.

30. Example of receptive profile

Level sets of receptive profiles can be recorded. It is an experimental "tour de force".

Here is an example from a cortical neuron in $V1$ (Gregory DeAngelis). The *elongation* of the profile explains the preferred orientation.

31. Example of receptive profile

Left: Level sets of ON (excitatory, red)/OFF (inhibitory, green) zones. Right: model using a third derivative $\varphi(x, y) = \frac{\partial^3 G}{\partial x^3}$).

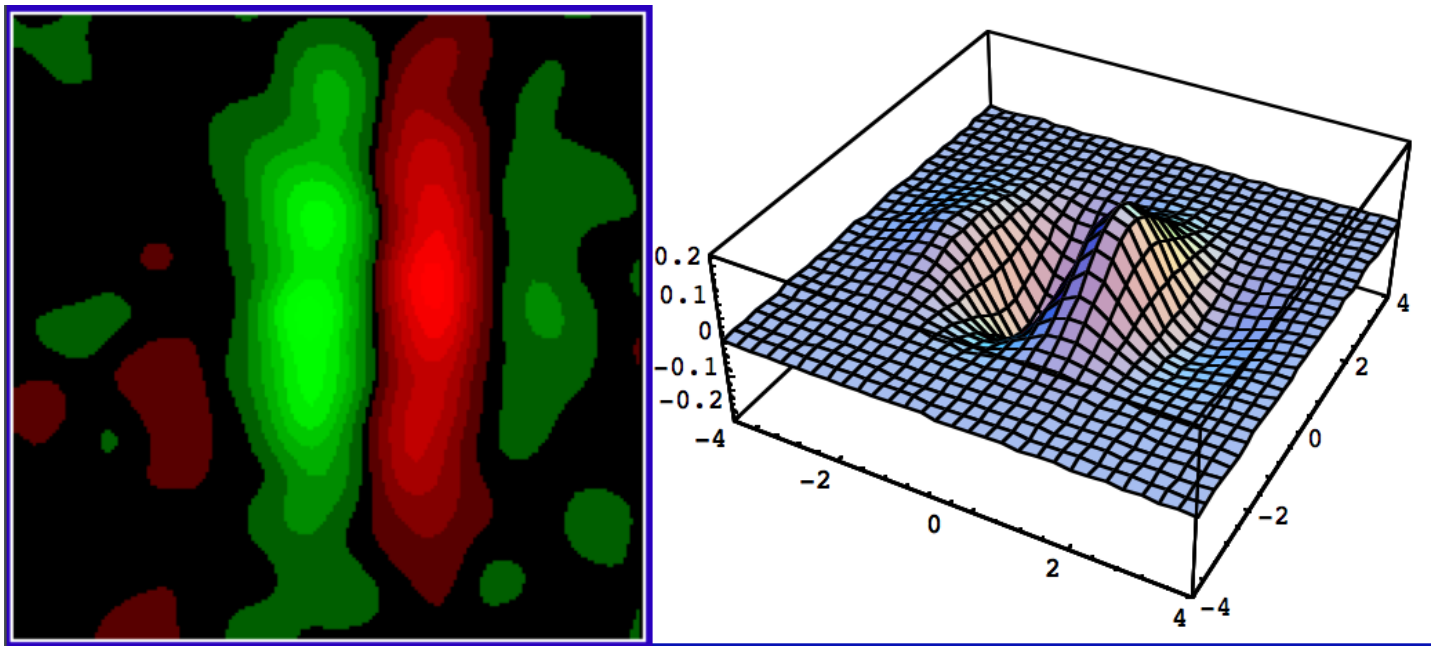

The filtering of the signal is like a *wavelet analysis*.

Wavelets are related to the notion of a *coherent state*.

You analyse signals in $L^2\left(\mathbb{R}^2\right)$ by considering a unitary irreducible square-integrable representation of the Euclidean group $SE(2)$ and taking the orbit of an "admissible" basic receptive profile φ_0.

The harmonic analysis of the signals using such coherent states enables to represent signals as superpositions of elementary functions and to *measure* them neurophysiologically.

33. Fields of detector cues

The second remark is that there are a lot of different types of receptive profiles adapted to the detection of different types of geometric cues: not only orientations, but also curvatures, inflexions, direction of motion, end-points, the orthogonal direction at an end-point, ocular dominance, phases, frequencies, crossings, etc.)

So we have *many fields* of specific receptive profiles "engrafted" (as said Hubel) over the retinal plane.

34. The "hard problem"

But now we run into a "hard problem".

The *geometry* of visual perception involves many *differential* computations. But neurons are (scaled) *point-like processors*. When they are actived, they emit spikes defining their "rate coding". And so, they can only code a single numerical value by means of their "firing rate".

Of course (i) they are able to detect complex point-like cues and (ii) they are connected and they can transmit their activity along their more or less inhibitory or excitatory connections.

But this is insufficient to *directly* implement differential routines.

35. The antinomy of perceptual geometry.

There is therefore an *antinomy* at the root of a neurally implemented perceptual geometry.

How differential routines can be neurally implemented in networks of "point-like processors" since derivatives are not point-like entities?

The classical conceptions of "differentiation" and "integration" do not work.

36. Functional connectivity

Now, we have seen that biological evolution has introduced *new* post-retinal modules and layers that implement *new* "engrafted" variables *beyond* the two variables of retinal position.

We can therefore try to understand how a connectivity *extended* to these new modules and layers can perform differential computations.

(i) It must certainly have a *very special* functional architecture.

(ii) But we must also know under what conditions a point-like functional architecture is able to implement a differential calculus. It is a *mathematical* problem.

37. The hypothesis

The hypothesis is therefore

Maybe point-like processors can implement an alternative formulation of differential calculus using "hidden derivatives" (Richard Montgomery) as new supplementary *independent* variables which can be implemented in point-like processors.

But these new "hidden" derivatives must satisfy strong *constraints* in order to be interpretable as "true" derivatives (as in Hamiltonian mechanics where you introduce the momenta as new *independent* variables and force them to be dual to velocities using the symplectic 2-form).

For that, *the hardwired connectivity of the network must be extremely specific*.

38. Alternative differential calculus

Now, alternative versions of differential calculus do exist in "modern" differential geometry since Pfaff, Jacobi, Frobenius, Lie, Darboux, Cartan, Goursat, etc.

They can solve the "hard problem" and it is why structures as jet-spaces, differential forms, contact structures, etc. are so basic in Neurogeometry,

To understand why, we must come back to this deep history of differential geometry.

39. Geometrizing integrability

The geometrization of the integrability conditions of differential equations has been a revolution (similar to that accomplished by Galois for the resolution of algebraic equations).

For a long time, the problem of the integration of differential equations $\omega = \sum_{i=1}^{i=n} A_i dx_i = 0$ was considered as "impossible", "absurd", "meaningless" if there was no integrating factor.

Gaspard Monge (1746-1818) was one of the first to explain (1784) that (in dimension 3) the conditions of integrability mean that the solutions of $\omega = 0$ are *surfaces* $F(x_i) = a$ in $\mathbb{R}^3$ but that, *even if the conditions are not satisfied*, there still exist "solutions" but which are 1D *skew curves* and no longer 2D surfaces.

40. Geometrizing integrability

From Pfaff to Frobenius differential geometers had gradually understood the condition of integrability $\omega \wedge d\omega = 0$.

Monge raised what became 30 years later the Pfaff problem and he prophesied its importance.

> *"It was not noticed that this was the beginning of an immense chain, to which lay the great difficulties of differential calculus."*

From that moment, geometrizing the integrability of differential equations became a hard problem.

41. Pfaff

Johann Friedrich Pfaff (1765-1825, the thesis advisor of Gauss) noted the difficulty of the problem.

He started from the work of the "sagacissimus" Lagrange and followed Monge's "egregia observatio" and explained that in order to move forward, he had to abandon ("deserere") the existing methods, and appeal to an "other principle" which "derives from the sources of the computation itself".

42. Pfaff

Pfaff emphasized that in a differential expression like $dz = pdx + qdy$ the partial derivatives p and q of $z(x, y)$ must be first considered as *new independent variables*, variables which can be interpreted as partial derivatives only in a second stage.

So, a basic notion became that of a *contact element* (Lie's "Flächen-element"), that is a pair of a point x of a manifold M and a hyperplane K_x of T_xM.

Sophus Lie developed this notion in great detail with a strong sense of the inversion of point of view it brought.

In a beautiful text of 1894 "The Geometric Work of Sophus Lie", Felix Klein emphasized the importance of the change of perspective brought about with this "new, clear and penetrating view".

He explained that, inspired by Monge and Plücker, Lie introduced "new elements of space" much more general than points and, instead of applying the methods of differential analysis to geometry, was interested in "the reciprocal" and developed "the application of geometrical intuition to Analysis".

This is the key foundational issue: the foundations of differential calculus moved from Analysis to Geometry.

And Klein insists:

> *"From these new points of view (...) the true meaning of the words "general", "complete", "singular" "solution" introduced by Lagrange and Monge, becomes extremely clear".*

46. The Pfaff problem. Frobenius

An essential conceptual step was made by Frobenius in his 1877 memoir "Über das Pfaff'sche Problem".

In particular, Frobenius introduced the "*bilinear covariant*" of a 1-form ω, which will be interpreted later by Cartan as the 2-form $d\omega$.

47. The Pfaff problem. Lie

In the years 1874-1878, Sophus Lie approached the problem from a different perspective, even more geometric and even less analytic.

In his 1877 memoir "Theorie des Pfaff'schen Problems", published the same year as that of Frobenius, he used the elements of contact and introduced his famous "tangential transformations" also called "contact transformations" ("Berührungstransformationen"). A contact transformation is a change of variables which leaves a PDE $\omega = 0$ *invariant*.

48. The Pfaff problem. Darboux

Like Lie and Frobenius, Gaston Darboux also explored Pfaff's theory, in particular in his 1882 memoir "Sur le problème de Pfaff". He was targeting the *intrinsic geometric structure* (invariant by changes of coordinates) of integrability.

> *"In this work I set out to explain the solution of Pfaff's problem without borrowing anything from the theory of partial differential equations and I mainly tried to highlight the invariance properties which play a fundamental role in this solution."*

The geometric turn from an analytic computation of integrals to geometric structure invariants became spectacular. The analogy with Galois is striking.

49. The geometric turn

We can thus see how a mixture of differential manifolds and multilinear antisymmetric algebra in tangent and cotangent spaces was set up. It allowed the geometrization of the integration of ODE and PDE.

As Chern and Chevalley pointed out in their 1952 obituary "Élie Cartan and his mathematical work" (Cartan died in 1951)

> *"The difficulty of conceiving the proper concepts at the early stage of development can hardly be overestimated."*

50. The Pfaff problem. Cartan

After this heroic period, Élie Cartan synthesized the major works on Pfaff's problem and created the theory of differential forms in two celebrated articles of 1899 and 1901 in the *Annales Scientifiques de l'École Normale Supérieure* :

"*Sur certaines expressions différentielles et le problème de Pfaff*" ,
"*L'intégration des systèmes d'équations aux différentielles totales*" .

51. The Pfaff problem

Édouard Goursat completed the theory in his 1922 treatise "*Leçons sur le problème de Pfaff*" .

Abstract geometrization became omnipresent. As was emphasized by Chern and Chevalley,

> *"the idea of studying the abstract structure of mathematical objects which hides itself beneath the analytical clothing under which they appear at first was also the mainspring of Cartan's theory of differential equations. [He] was able to see the geometrical content of very complicated calculations."*

52. Three geometric traditions

In his 1936 lecture at the ICM (Oslo), Cartan commented on the

> *"three main points of view which have dominated the evolution of geometry."*

1. Klein: invariance w.r.t. a given group.
2. Riemann: metric tensor.
3. "Parallelism" and "parallel transport": connections on fiber bundles (his own conception).

The problem is to connect between them the neighboring fibers when one moves in the base M. As noted again by Chern and Chevalley, it is

> *"to tie up the fibers with the differentiable structure of the base space."*

53. "Point-like processors" can be good geometers

But, it is exactly the case of the hypercolumns of $V1$ tied up as fibers with the retinal base plane.

So, we see that "point-like processors" can be good differential geometers if they are able to detect contact elements.

54. The main hypothesis

Hence the main hypothesis:

while the retinal cells detect positions, cortical neurons of $V1$ can detect contact elements and their cortico-cortical connectivity can implement a "geometry of integrability" for these contact elements.

To understand at the neurophysiological level how the visual system can implement an integro-differential calculus, we must therefore understand at the mathematical level how an integro-differential calculus can be equivalent to a geometry of connectivity between contact elements.

In that sense, the visual brain is a Cartan engine.

55. The first example: $V1$

In the 1990s I developed the following relations between neurophysiology and geometry:

1. a class of cortical neurons in $V1$ (called "simple") detect contact elements (a, p) where a are positions on the retina and p a local orientation at a (Hubel and Wiesel);
2. the fibration $(a, p) \longrightarrow a$ is neurophysiologically implemented by retinotopy and orientation hypercolumns;
3. the contact structure of the 1-jets of plane curves is neurophysiologically implemented (horizontal cortico-cortical connections);
4. the sub-Riemannian geometry of this contact structure is neurophysiologically implemented (illusory contours as geodesics).

For elaborating this first model I had the privilege to collaborate with eminent specialists of neurosciences, physiology and psychophysics as Michel Imbert, Alain Berthoz, Yves Frégnac, and Jean Lorenceau.

With them and colleagues as Bernard Teissier, David Mumford, Daniel Bennequin, Jean-Michel Morel, Stéphane Mallat, Olivier Faugeras, Giuseppe Longo, we organized in the 1990s a lot of seminars and conferences e.g. at the "Fondation des Treilles", at the Institut Henri Poincaré, at Oberwolfach, at the École Normale Supérieure, and at the Collège de France.

In the 2000s these works continued to be worked out. I edited with Jean Lorenceau a double special issue of the *Journal of Physiology-Paris* (Yves Frégnac was the Editor-in-Chief).

57. Geometry and neurophysiology

Each of the propositions of the model refers to crucial neurophysiological discoveries which are all experimental "tours de force".

That biological evolution has been able to lead, from simple peripheral photosensitive sensors, to such genetically controlled *cortical* structures implementing sophisticated *geometrical* structures is a real miracle.

A striking example is retinotopy, which is geometrically trivial (a fibration) but neurophysiologically incredibly complex.

58. Axon guidance and chemotaxis

The genetic control of retinotopy is a fascinating morphogenetic process.

It requires extremely accurate targeting and axon guidance.

A key mechanism is *axon chemotaxis*, which occurs through gradients of chemo-attractive and chemo-repulsive molecules like the "ephrins".

Eph receptors (receptor tyrosine kinases) and their ephrin ligands are essential mediators of cell-cell communication. They regulate cell attachment, shape, and mobility.

There is an "address system" of molecular tags which determines the specificity of the axon connections in topographical maps.

59. Eph / ephrin gradients

The following figure due to Benjamin Reese schematizes the gradient-controlled dynamics for the retina $\longrightarrow$ tectum projection in the non mammalian brain of the chicken (the optic tectum is the analogous of the superior colliculus in mammals).

It is much simpler than the projection $LGN \longrightarrow V1$ but is already a fine example.

It shows how the increasing naso$\nearrow$temporal ($N \nearrow T$) *EphA* and dorso$\nearrow$ventral ($D \nearrow V$) *EphB* gradients of the ganglion cell layer allows the axon growth cone of these cells to reach a precise position in the tectum defined by the increasing complementary gradients of rostro-caudal ($R \nearrow C$) *ephrin-A* and lateromedial ($L \nearrow M$) *ephrin-B* with opposite *EphA* and *EphB* gradients.

60. Reese's image

The retinotopic map $N \to C$, $T \to R$, $D \to L$, $V \to M$.

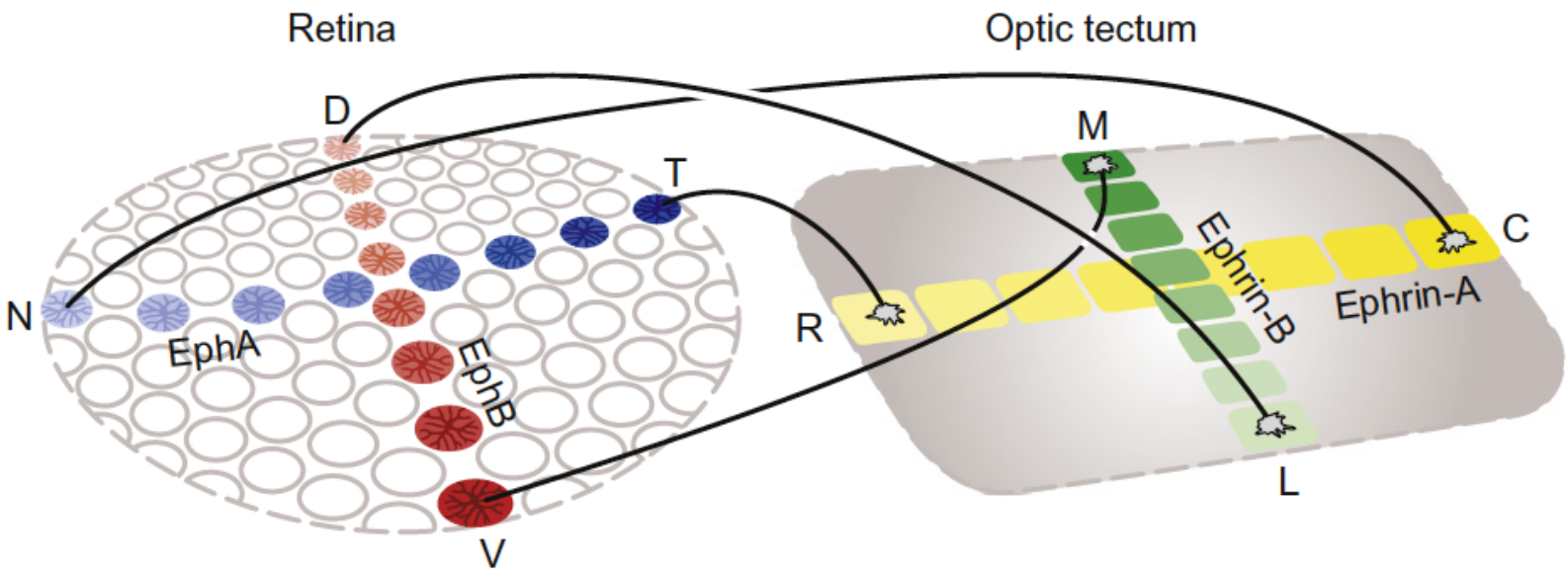

61. From local cues to global geometry

So, we have to understand how this very complex neurophysiology of visual neurons detecting *local* cues can generate the *global geometry* of the perceived images, with all the well-known phenomena studied since Gestalt theory, e.g. *long range illusory contours*.

Long range illusory contours are one of the most striking phenomenon of low level vision.

We can reconstruct the shape of a dalmatian dog in this very incomplete image:

62. Illusory contours

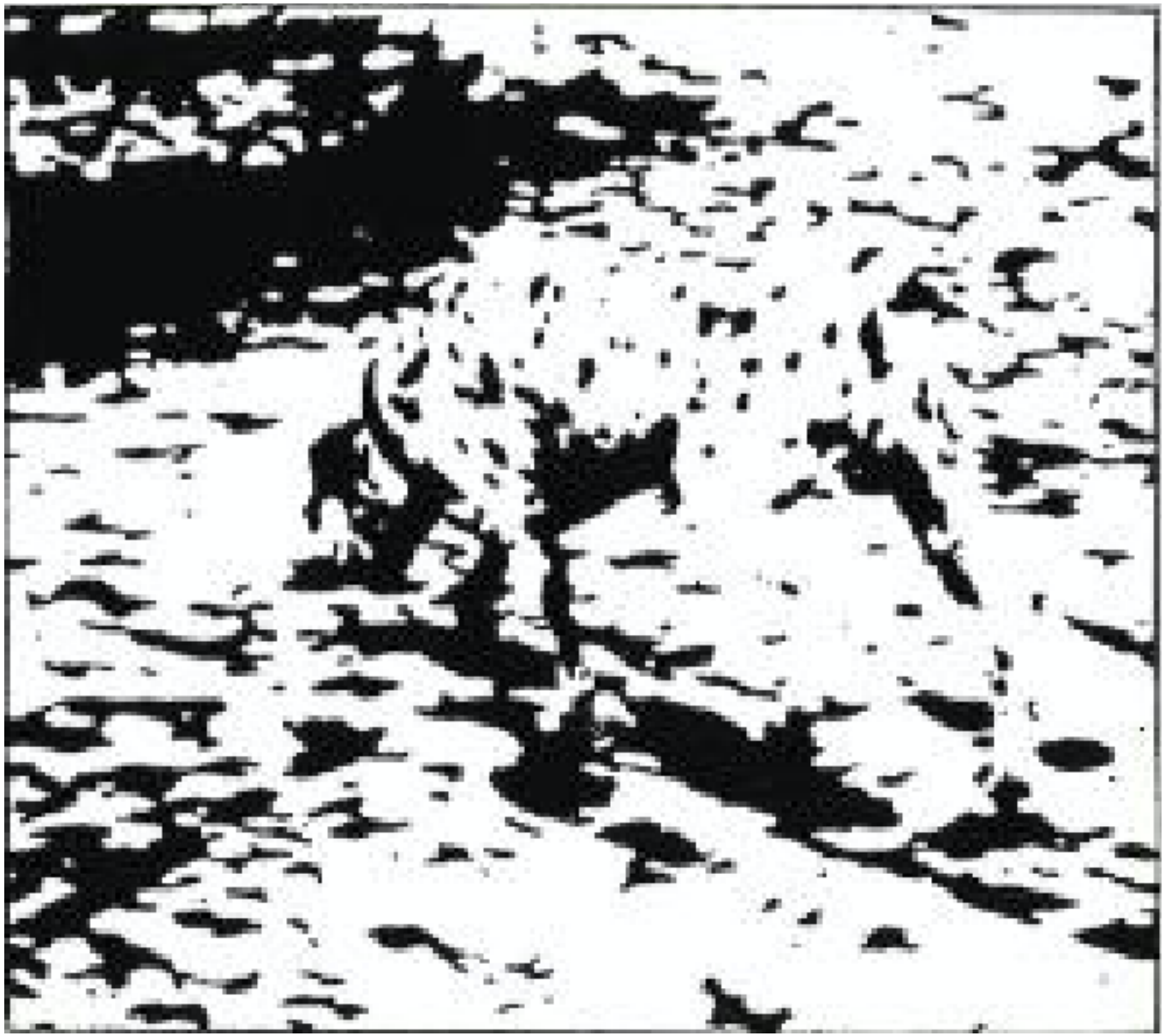

63. Illusory contours as geodesics

We will see that they can be interpreted as *geodesics* of a contact structure for an appropriate metric.

Such sub-Riemannian models have many applications, in particular for *inpainting*, since to complete a corrupted image, we must construct the *illusory level sets* that can complete the missing parts.

64. An example of sub-Riemannian inpainting

The following picture shows how a highly corrupted image (left) can be very well restored using sub-Riemannian diffusion (Gauthier-Prandi inpainting based on our model).

The face of our friend Jean-Paul Gauthier appears out of the blue.

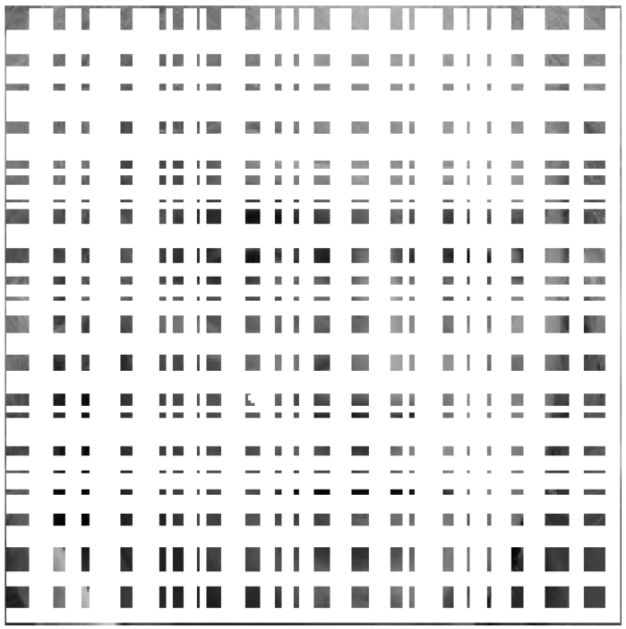

65. The functional architecture

Let us explain now the way to sub-Riemannian models.

As we have seen, simple neurons of $V1$ are parametrized by triples (a, p) where $a = (x, y)$ is a position on the retina (identified with $\mathbb{R}^2$) and p is an orientation (modulo π) at a.

66. "Hidden derivatives"

But the fibration $\mathbb{V} = \mathbb{R}^2 \times \mathbb{P}^1 \longrightarrow \mathbb{R}^2, (a, p) \mapsto a$ is not sufficient for interpreting p as an "hidden derivative" (Richard Montgomery), that is as a tangent to a curve.

For that, p must satisfy the fundamental Pfaff equation $\omega = dy - pdx = 0$ defining the contact structure of 1-jets of plane curves.

67. The contact structure of 1-jets

Indeed, a skew curve

$$\Gamma = v(s) = (a(s), p(s)) = (x(s), y(s), p(s))$$

in $\mathbb{V}_J$ is the *Legendrian lift* of its projection $\gamma = a(s)$ onto the base plane $\mathbb{R}^2$

- iff the "hidden" derivative $p(s)$ is the "real" derivative $p = dy/dx$ giving the tangent to the base curve γ at the point $a(s)$,
- iff it is an *integral curve* of the *contact structure* $\mathcal{C} = ker(\omega)$ of $\mathbb{V}_J$, where ω is the 1-form

$$\omega = dy - pdx$$

68. The distribution of contact planes

The distribution $\mathcal{C}$ of contact tangent planes is maximally non integrable since the 3-form

$$\omega \wedge d\omega = (-pdx + dy) \wedge dx \wedge dp = -dx \wedge dy \wedge dp \ .$$

is a volume form, which is the opposite of the Frobenius integrability condition $\omega \wedge d\omega = 0$.

So, even if there exists a lot of integral *curves* of $\mathcal{C}$ (Legendrian lifts), there exists no integral *surface*.

What Monge had prophesied!

69. The (polarized) Heisenberg group

Let's remember that the contact structure $\mathcal{C}$ is left-invariant for a group law making $\mathbb{V}_J$ isomorphic to the (*polarized*) *Heisenberg group* $\mathbb{H}_{pol}$.

$$(x, y, p).(x', y', p') = (x + x', y + y' + px', p + p') \ .$$

Its Lie algebra is generated by the basis of left-invariant fields $X_1 = \frac{\partial}{\partial x} + p\frac{\partial}{\partial y} = (1, p, 0)$ and $X_2 = \frac{\partial}{\partial p} = (0, 0, 1)$ with $[X_1, X_2] = (0, -1, 0) = -\frac{\partial}{\partial y} = -X_3$ (the other brackets $= 0$).

The basis $\{X_1, X_2\}$ of the distribution $\mathcal{C}$ is *bracket generating* (*i.e.* Lie-generates the whole tangent bundle $T\mathbb{V}_J$) (Hörmander condition).

$\mathbb{V}_J = \mathbb{H}_{pol}$ is a *nilpotent* group of step 2 (a Carnot group).

70. The contact structure of $SE(2)$

This can be generalized to the Euclidean group $SE(2)$.

The contact form of $SE(2)$ is

$$\omega_S = \cos(\theta)\, dy - \sin(\theta)\, dx$$

The contact planes are spanned by the tangent vectors $X_1 = \cos(\theta)\frac{\partial}{\partial x} + \sin(\theta)\frac{\partial}{\partial y}$ and $X_2 = \frac{\partial}{\partial \theta}$ with Lie bracket $[X_1, X_2] = \sin(\theta)\frac{\partial}{\partial x} - \cos(\theta)\frac{\partial}{\partial y} = -X_3$ (Reeb vector field).

71. The two models

The distribution $\mathcal{C}$ of contact planes is still bracket generating (Hörmander condition). But $SE(2)$ is no longer nilpotent. The Carnot group $\mathbb{V}_J = \mathbb{H}_{pol}$ is its "*tangent cone*", its "nilpotentisation".

72. Neural contact structure

The very key point, which is another striking *experimental* discovery, is that the contact structure of $\mathbb{V}$ is *implemented* in a *specific class* of neural connections.

Orientation hypercolumns correspond to the "vertical" retino-geniculo-cortical connectivity.

But cortical neurons of $V1$ are also connected by "horizontal" cortico-cortical connections *inside the cortical layer itself*.

They are long-ranged (up to 6-8 mm), excitatory, slow (about $0.2\,\mathrm{m}\,/\,\mathrm{s}$) and distributed in a very anisotropic and "patchy" way. It is the key point.

73. Necessity of a parallel transport

Such a second system of long-range "horizontal" cortico-cortical connections is necessary to implement a *parallel transport* enabling the visual system to *compare* two retinotopically neighboring orientation hypercolumns P_a and P_b over two different base points a and b.

These long-range "horizontal" cortico-cortical connections implement a "Cartan hardware".

As claimed William Hoffman in a pioneering paper of 1989, "the visual cortex is a contact bundle".

74. The key result

The key experimental discovery is that

"the system of long-range horizontal connections can be summarized as preferentially linking neurons with co-oriented, co-axially aligned receptive fields." (W. Bosking)

This means that a chain of simple neurons (a_i, p_i) is a chain of *"horizontally" connected* simple neurons iff it is a discretization of the Legendrian lift of a not too curved base curve interpolating between the (a_i).

So, this means that,

up to some bound on curvature, the contact structure $\mathcal{C}$ is neurally implemented in $V1$.

75. Joint position–orientation constraints

Deep experiments of *psychophysics* (Field, Hayes and Hess) concluded also that the *specific connectivity* of $V1$ is characterized by "joint conditions on positions and orientations", which implement one of the fundamental laws of Gestalt theory, that of "good continuation" ("Gesetz der guten Fortsetzung")

1. two elements (a_1, p_1) and (a_2, p_2) are connected if one can *interpolate* between them a curve γ (which is tangent to p_1 and p_2 at a_1 and a_2, respectively) that is not too curved; between positions a_1 and a_2, and which is tangent to p_1 and p_2 at a_1 and a_2, respectively;
2. otherwise the two elements are not connected.

These "joint constraints on positions and orientations" correspond to neural horizontal cortico-cortical connections.

76. 2-jets and Engel structure

This type of approach can be extended to higher order jets. For example for 2-jets, we introduce a 4th independent variable κ for the curvature and, on $\mathbb{R}^4$, in addition to the contact form $\omega_J = dy - pdx$, we introduce the additional Pfaff form $\tau_J = dp - \kappa dx$ expressing its interpretation as curvature. We get the Engel group with the following law :

$$\begin{aligned} & (x, y, p, \kappa)\left(x', y', p', \kappa'\right) \\ = \quad & \left(x + x', y + y' + px', p + p', \kappa + \kappa' + yx' + \frac{1}{2}px'^2\right) \end{aligned}$$

77. Two vocabularies

So, we get a correspondance between two vocabularies, a neurophysiological one and a mathematical one.

simple neurons	(scaled) contact elements (a, p)
R-G-C retinotopy	base space $\mathbb{R}^2$ of positions a
basic / "engrafted" variables	fiber bundle $\mathbb{R}^2 \times P \to \mathbb{R}^2$
orientation hypercolumns and pinwheels	1-jet space $J^1 \subsetneq \mathbb{R}^2 \times P \to \mathbb{R}^2$
◇ long-range horizontal connections, ◇ "co-oriented, co-axially aligned RFs", ◇ "joint constraints on positions and orientations" ◇ "good continuation"	Contact structure

78. Variational models for illusory contours

Now, let us come back to *curved* illusory contours. *Variational models* have been introduced since the late 70s.

1. Shimon Ullman (1976) explained that

   "A network with the local property of trying to keep the contours 'as straight as possible' can produce curves possessing the global property of minimizing total curvature."

2. Berthold Horn introduced in 1983 "the curves of least energy".

These models minimize an energy along curves *in the base plane*.

79. Mumford's elastica model. I

The best known is the *elastica* model proposed in 1992 by David Mumford.

The energy to minimize is:

$$E = \int_\gamma (\alpha\kappa^2 + \beta) ds$$

where γ is a smooth curve in $\mathbb{R}^2$.

The problem was first raised by Jacques Bernouilli and then his nephew Daniel Bernouilli who proposed it to Euler in a letter (1742). Euler solved it in his fantastic *Addendum: De Curvis elastica* to his *Methodus* of 1744, the founding text of the Calculus of Variations.

80. Mumford's elastica model. II

Mumford argued that an illusory contour is a chain of pairs (a_i, p_i) along which the loss of activity is as weak as possible.

But leaks can have a double origin:

1. leaks proportional to the number of elements of the chain lead to the term $\int_\gamma \beta ds$ with a constant factor β;
2. leaks due to curvature and equal to the sum of the deflections of orientation between consecutive elements lead to the term $\int_\gamma \alpha \kappa^2 ds$

81. Geodesic models

But for *neural* models (and not only 2D image processing) it is natural to work in $V1$, that is with the *contact structure* and the *Legendrian lifts*.

It is here that sub-Riemannian geometry fully comes on stage.

The natural idea is to introduce sub-Riemannian metrics on $\mathbb{V}$ and look at geodesic models for curve completion and illusory modal contours.

82. Sub-Riemannian metrics

We take the natural basis $\{X_1, X_2\}$ of the contact plane at the origin as an *orthonormal* basis and we *translate* it using left translations. As the contact structure is left-invariant, we get that way a left-invariant metric on the contact planes.

As this metric is defined only on the contact planes and not on the complete tangent spaces it is sub-Riemannian. But it enables to compute the length of the integral curves of the contact structure, that is of Legendrian lifts.

In the 2000s these problems have been further explored.

(i) Alessandro Sarti and Giovanna Citti began to be interested in Neurogeometry. They organized many important international symposia in Bologna (2004, 2009) and Pisa (Scuola Normale Superiore, 2006). We edited together in 2009 another double special issue of the *Journal of Physiology-Paris* and developed a very fruitful collaboration.

(ii) I had the privilege to meet Andrei Agrachev of the SISSA and other very fruitful cooperation on sub-Riemannian geometry quickly started with members of his group, in particular Jean-Paul Gauthier, Ugo Boscain and Yuri Sachkov.

84. The sub-Riemannian $\mathbb{H}_{pol}$

The sub-Riemannian geometry (geodesics, conjugate points, cut locus) of groups such as $\mathbb{H}_{pol}$ or $SE(2)$ is rather complex, even if the groups are elementary.

The sub-Riemannian geometry of the Heisenberg group $\mathbb{H}$ has been explained in the 1980s by Richard Beals, Bernard Gaveau and Peter Greiner.

It can easily be adapted to the polarized $\mathbb{H}_{pol}$.

85. The sub-Riemannian Hamiltonian

The sub-Riemannian sphere S and the wave front W are rather strange. One can compute them explicitly .

Due to the Pontryagin maximum principle, geodesics are the projections on $\mathbb{H}_{pol}$ of the trajectories of a Hamiltonian field defined on the cotangent space.

$$H(x, y, p, \xi^*, \eta^*, \pi^*) = \frac{1}{2}\left[(\xi^* + p\eta^*)^2 + \pi^{*2}\right] \ .$$

where $(x, y, p) = q$ are coordinates in $\mathbb{H}_{pol}$ and (ξ^*, η^*, π^*) coordinates in the cotangent space $T^*_q\mathbb{H}_{pol}$.

86. The sub-Riemannian wavefront of $\mathbb{H}_{pol}$

Using the variable $\varphi = \frac{\eta_0^* \tau}{2}$ associated to the length τ of the geodesic and the constant moment η_0, the sphere $S(0, R)$ and the wave front $W(0, R)$ of $\mathbb{H}_{pol}$ are given by the following equations (where θ is the angle of the tangent).
(x, p) are expressed in polar coordinates with module $\frac{|\sin(\varphi)|}{\varphi}$, $\varphi > 0$.

$$\begin{cases} x_1 = \frac{|\sin(\varphi)|}{\varphi} \cos(\theta) \\ p_1 = \frac{|\sin(\varphi)|}{\varphi} \sin(\theta) \\ y_1 = \frac{1}{2} x_1 p_1 + \frac{\varphi - \sin(\varphi)\cos(\varphi)}{4\varphi^2} \\ = \frac{1}{2} \frac{\sin^2(\varphi)}{\varphi^2} \cos(\theta) \sin(\theta) + \frac{\varphi - \cos(\varphi)\sin(\varphi)}{4\varphi^2} \\ = \frac{\varphi + 2\sin^2(\varphi)\cos(\theta)\sin(\theta) - \cos(\varphi)\sin(\varphi)}{4\varphi^2} \end{cases}$$

87. Image of the SR sphere of $\mathbb{H}$

They are displayed in the following figure. The external surface is the sub-Riemannian sphere S. It has a saddle form with singularities at the intersections with the y-axis.

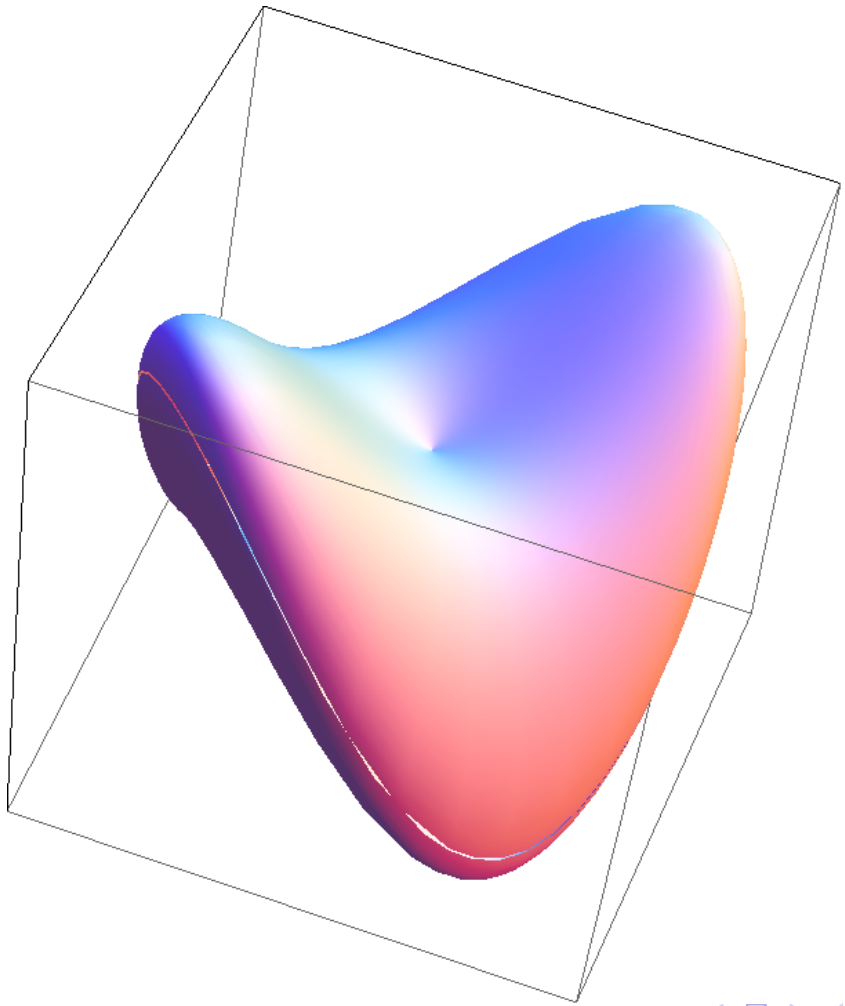

88. Image of the wave-front of $\mathbb{H}$

The internal part is $W - S$. It presents smaller and smaller circles of cusp singularities which converge to 0. Such a complex behavior is impossible in Riemannian geometry.

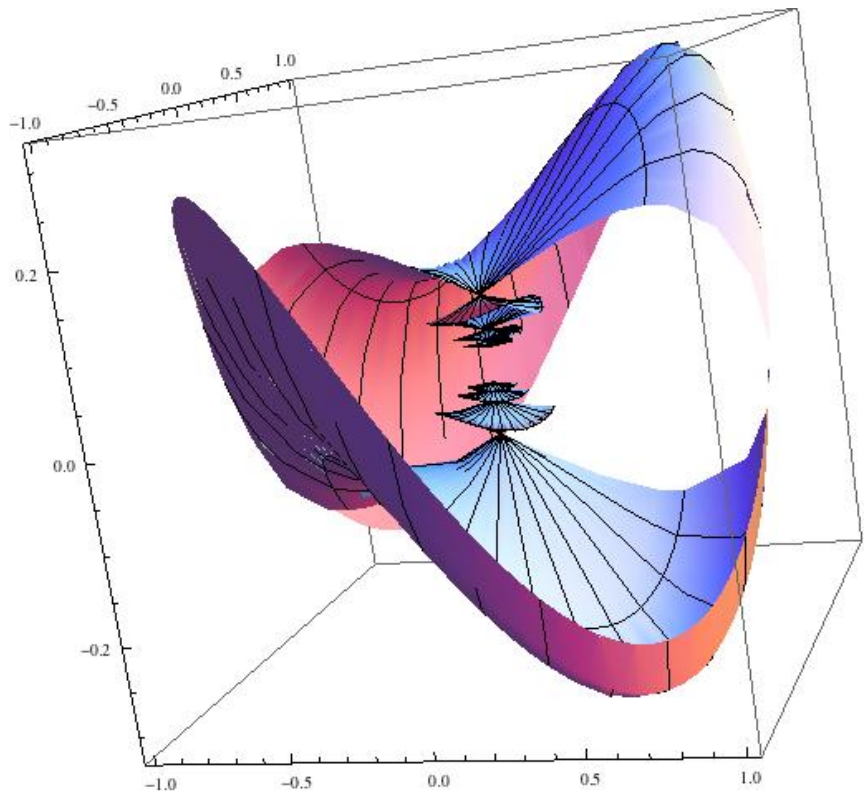

89. The cusps of W

The following figure displays the quarter of the wave front W for $\theta = 0$. Its equations are $x_1 = \frac{|\sin(\varphi)|}{\varphi}$, $p_1 = 0$, $y_1 = \frac{\varphi - \cos(\varphi)\sin(\varphi)}{4\varphi^2}$.
The cusps are on the curve of equation $x = \cos(\varphi)$,
$y = \frac{1}{4}\cos(\varphi)\sin(\varphi)$.

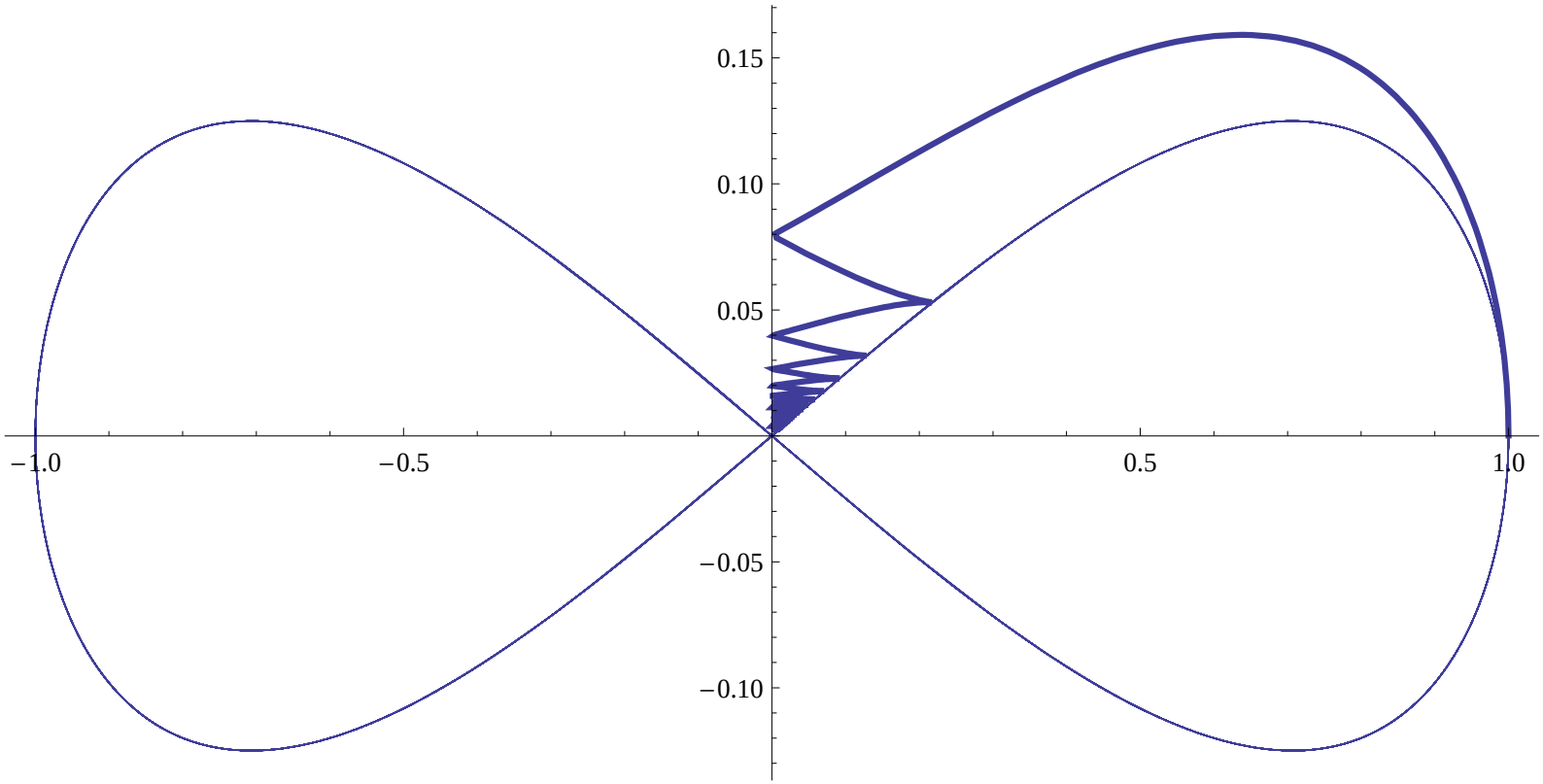

90. The example of $SE(2)$

With Giovanna Citti and Alessandro Sarti we studied the passage from the $\mathbb{V}_J$ bundle, with its natural action of the Euclidean group $\mathbb{R}^2 \rtimes \mathbb{S}^1 = SE(2)$, to $SE(2)$ itself.

We thus go to the model $SE(2) = \mathbb{V}_S$ endowed with its natural contact structure and its associated L-invariant sub-Riemannian metric.

The geometry of the sub-Riemannian spheres and wavefronts is much more complicated. It was computed in the 2000s by Andrei Agrachev, Yuri Sachkov, Igor Moiseev, Ugo Boscain, Jean-Paul Gauthier.

91. The Hamiltonian of $SE(2)$

We have seen that the contact 1-form is $\omega_S = \omega = -\sin(\theta)\,dx + \cos(\theta)\,dy$ and the basis of contact planes is $X_1 = \cos(\theta)\,\partial_x + \sin(\theta)\,\partial_y$ and $X_2 = \partial_\theta$ with Lie bracket $[X_1, X_2] = \sin(\theta)\,\partial_x - \cos(\theta)\,\partial_y = X_3$, and $-X_3$ being the Reeb field.

If λ_1, λ_2, λ_3 are the components of the covector λ in the basis $(\omega_1, \omega_2, \omega_3)$ dual to (X_1, X_2, X_3) (i.e. $\lambda_i = \langle \lambda, X_i \rangle$), the Hamiltonian giving the geodesics is

$$H(\lambda, q) = \frac{1}{2}\left(\lambda_1^2 + \lambda_2^2\right)$$

H is constant along trajectories. If $H = \frac{1}{2}$, and if we take $\lambda_1 = \sin\left(\frac{\gamma}{2}\right)$, $\lambda_2 = -\cos\left(\frac{\gamma}{2}\right)$, then γ satisfies the *pendulum equation*

$$\ddot{\gamma} = -\sin(\gamma)$$

and Hamilton equations become

$$\begin{cases} \dot{x} = \sin\left(\frac{\gamma}{2}\right)\cos(\theta) = \lambda_1\cos(\theta) \\ \dot{y} = \sin\left(\frac{\gamma}{2}\right)\sin(\theta) = \lambda_1\sin(\theta) \\ \dot{\theta} = -\cos\left(\frac{\gamma}{2}\right) = \lambda_2 \\ \ddot{\theta} = \frac{1}{2}\sin\left(\frac{\gamma}{2}\right)\dot{\gamma} = \dot{\lambda}_2 \end{cases}$$

93. The control pendulum

The energy of the pendulum is
$E = \frac{1}{2}(\dot{\gamma})^2 - \cos(\gamma) = \frac{1}{2}(c)^2 - \cos(\gamma)$. Its minimum is -1.

The phase portrait $\mathcal{C}$ of the pendulum is given by the level lines of E. It is stratified and and decomposes into strata of respective dimensions 2, 1, 0 (i.e. of codimension 0, 1, 2).

Its stratification drives the classification of geodesics. (the fact that γ has period 4π is important).

94. The pendulum phase portrait

In magenta: open stratum C_1 (2 connected components, oscillations). In yellow: open stratum C_2 (2 connected components, rotation). In thick lines: the 1-dimensional stratum C_3 (4 connected components). Point strata C_4 (2 points, stable equilibrium) and C_5 (2 points, unstable equilibrium).

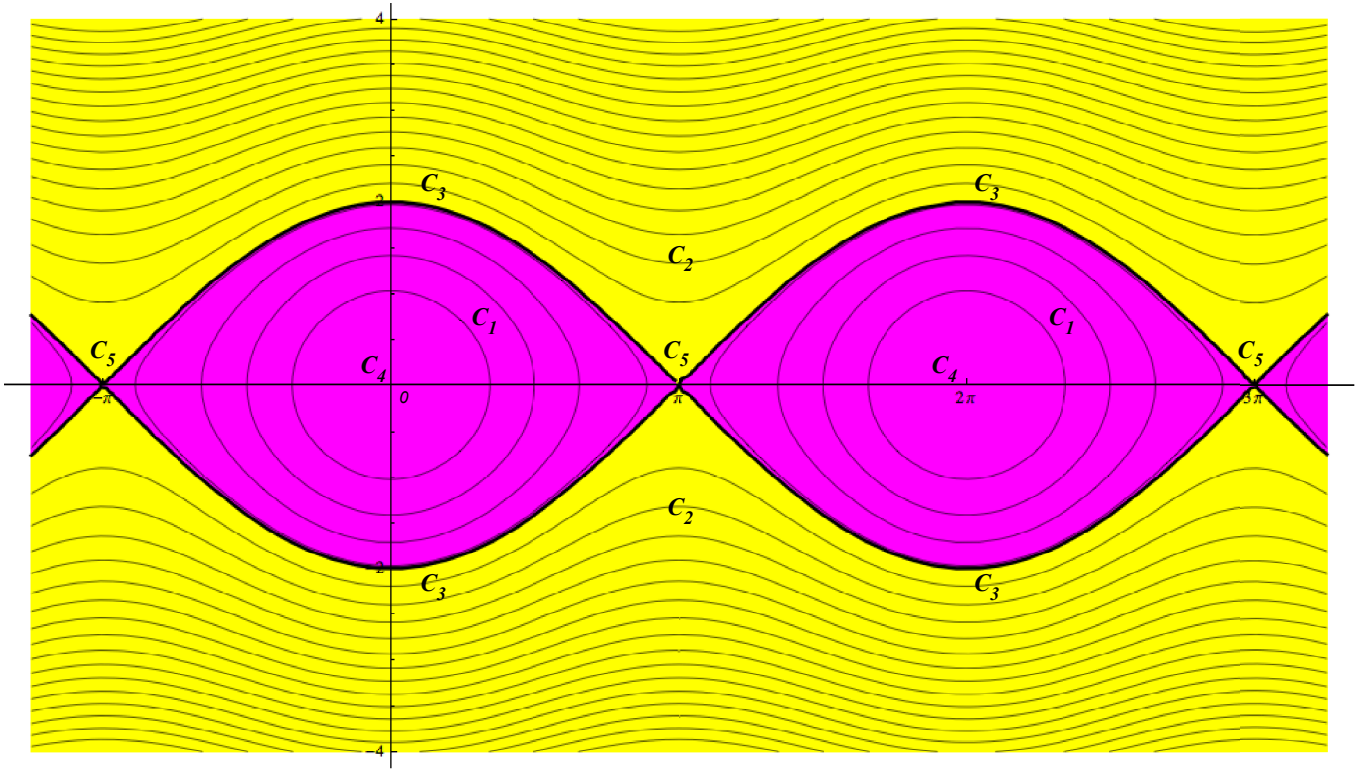

95. Jacobi coordinates

Sachkov then computed the sub-Riemannian geometry of $\mathbb{V}_S = SE(2)$ using *Jacobi coordinates* (φ, k) which "rectify" the dynamics of the pendulum $\ddot{\gamma} = -\sin(\gamma)$.

In these coordinates, the "vertical" system in the fibers becomes trivial because $\dot{k} = 0$ and $\dot{\varphi} = 1$, i.e. $\varphi_t = \varphi + t$ with $\varphi = \varphi_0$. k is the modulus of the elliptic integral associated with the pendulum: it encodes the energy E; φ is the "pendular" time-length: it encodes the length of the geodesic.

96. $SE(2)$ geodesic equations

For the C_1^0 stratum, Sachkov and Moiseev found (with $x_t = x(t)$, etc., and $\mathbb{E}(\varphi) = E(\mathrm{am}(\varphi), k) = \int_0^\varphi \mathrm{dn}^2(r, k)\, dr$), E being the elliptic integral of the second kind):

$$\begin{cases} c = 2k\,\mathrm{cn}(\varphi, k) \\ \sin\left(\frac{\gamma}{2}\right) = k\,\mathrm{sn}(\varphi, k) \text{ and } \cos\left(\frac{\gamma}{2}\right) = \mathrm{dn}(\varphi, k) \\ \cos(\theta_t) = \mathrm{cn}(\varphi, k)\,\mathrm{cn}(\varphi_t, k) + \mathrm{sn}(\varphi, k)\,\mathrm{sn}(\varphi_t, k) \\ \sin(\theta_t) = \mathrm{sn}(\varphi, k)\,\mathrm{cn}(\varphi_t, k) - \mathrm{cn}(\varphi, k)\,\mathrm{sn}(\varphi_t, k) \\ x_t = \frac{1}{k}\left(\mathrm{cn}(\varphi, k)\left(\mathrm{dn}(\varphi, k) - \mathrm{dn}(\varphi_t, k)\right) + \mathrm{sn}(\varphi, k)\left(t + \mathbb{E}(\varphi) - \mathbb{E}(\varphi_t)\right)\right) \\ y_t = \frac{1}{k}\left(\mathrm{sn}(\varphi, k)\left(\mathrm{dn}(\varphi, k) - \mathrm{dn}(\varphi_t, k)\right) - \mathrm{cn}(\varphi, k)\left(t + \mathbb{E}(\varphi) - \mathbb{E}(\varphi_t)\right)\right) \\ \theta_t = \mathrm{am}(\varphi) - \mathrm{am}(\varphi_t) \mod (2\pi) \end{cases}$$

They are composed with Jacobi elliptic functions of φ and $\varphi_t = \varphi + t$.

There exist similar formulas for the other strata.

97. The SR spheres $S(0,R)$ and wavefronts $W(0,R)$ of $SE(2)$

The sub-Riemannian spheres $S(0,R)$ and wavefronts $W(0,R)$, $S(0,R) \subset W(0,R)$, of $\mathbb{V}_S = SE(2)$ look a bit like those of the polarized Heisenberg group, but are much more complicated.

The fundamental difference is that the y-axis, which was a degenerate caustic in the $\mathbb{V}_J$ case, splits into four cusp branches of an astroidal cone and the point singularities on the y-axis in the $\mathbb{V}_J$ case unfold into small "tetrapaks".

We illustrate first the case $R = \frac{\pi}{2}$. The strata C_i are sent by the exponential map into strata $W_{C_i,\frac{\pi}{2}}$ of $W\left(0,\frac{\pi}{2}\right)$. The following figure displays two viewpoints on $W_{C_1,\frac{\pi}{2}}$ as well as $W_{C_3,\frac{\pi}{2}}$.

98. $W_{C_{1\&3},\frac{\pi}{2}}$

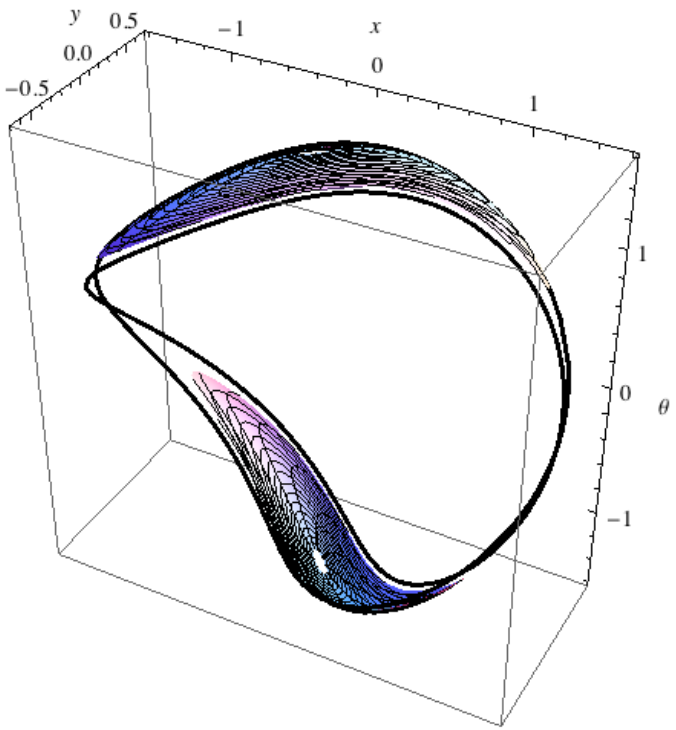

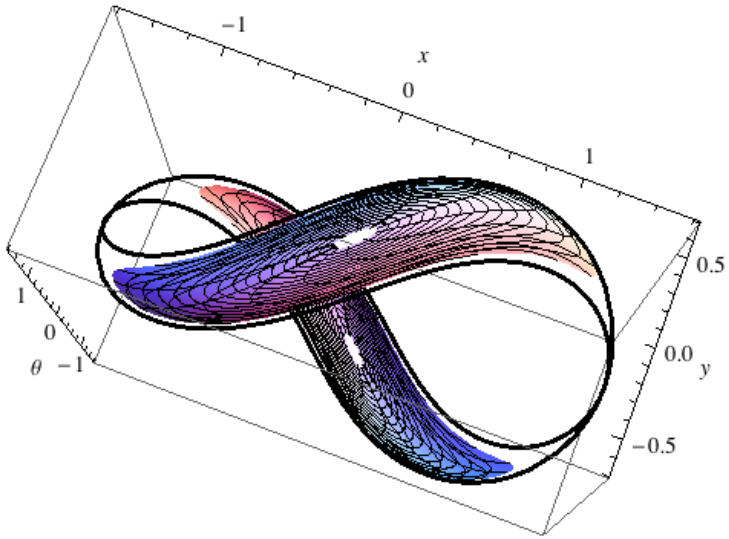

The images of the $C_2^{\pm}$ strata are much more complicated, with an infinity of singularities accumulating on the origin.

Let us consider the image $W_{C_2^+,\frac{\pi}{2}}$ of C_2^+ with its level lines L_k for $k = \text{cst}$. The figure shows some of them from two viewpoints. They are twisted circles with highly oscillating mean "radius"converging to 0.

100. $W_{C_2^+, R=\frac{\pi}{2}}$

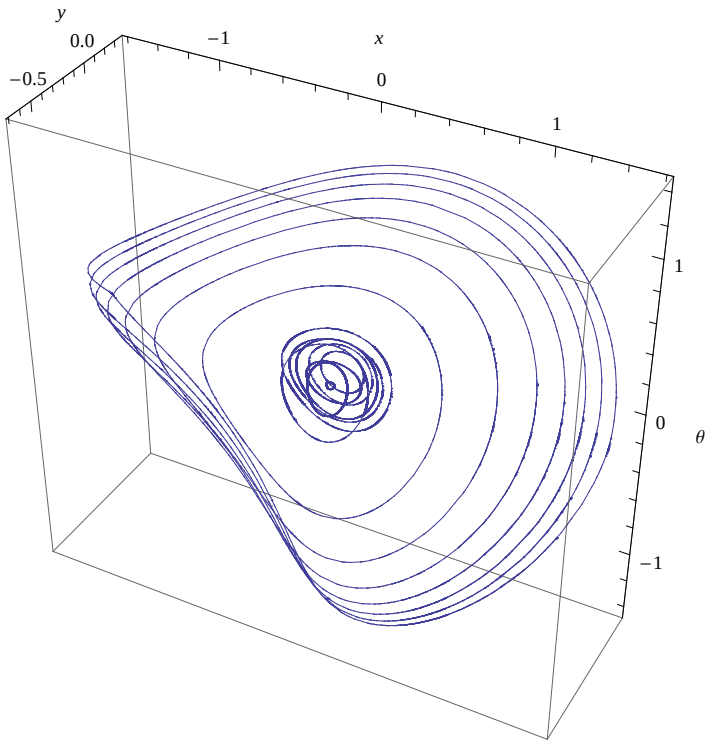

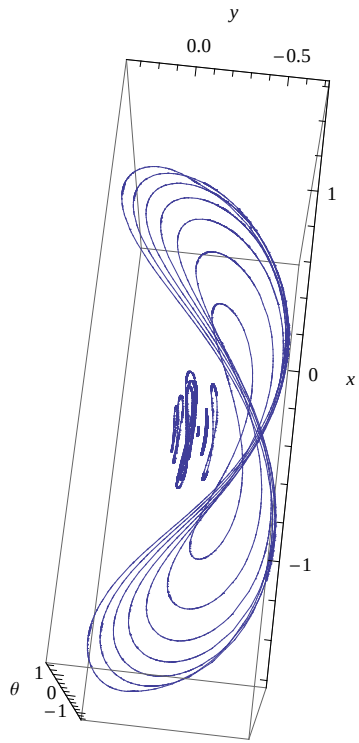

101. $W_{C_2^+,R=\frac{\pi}{2}}$

$W_{C_2^+,\frac{\pi}{2}}$ for $k \in (0.07, 0.8)$.

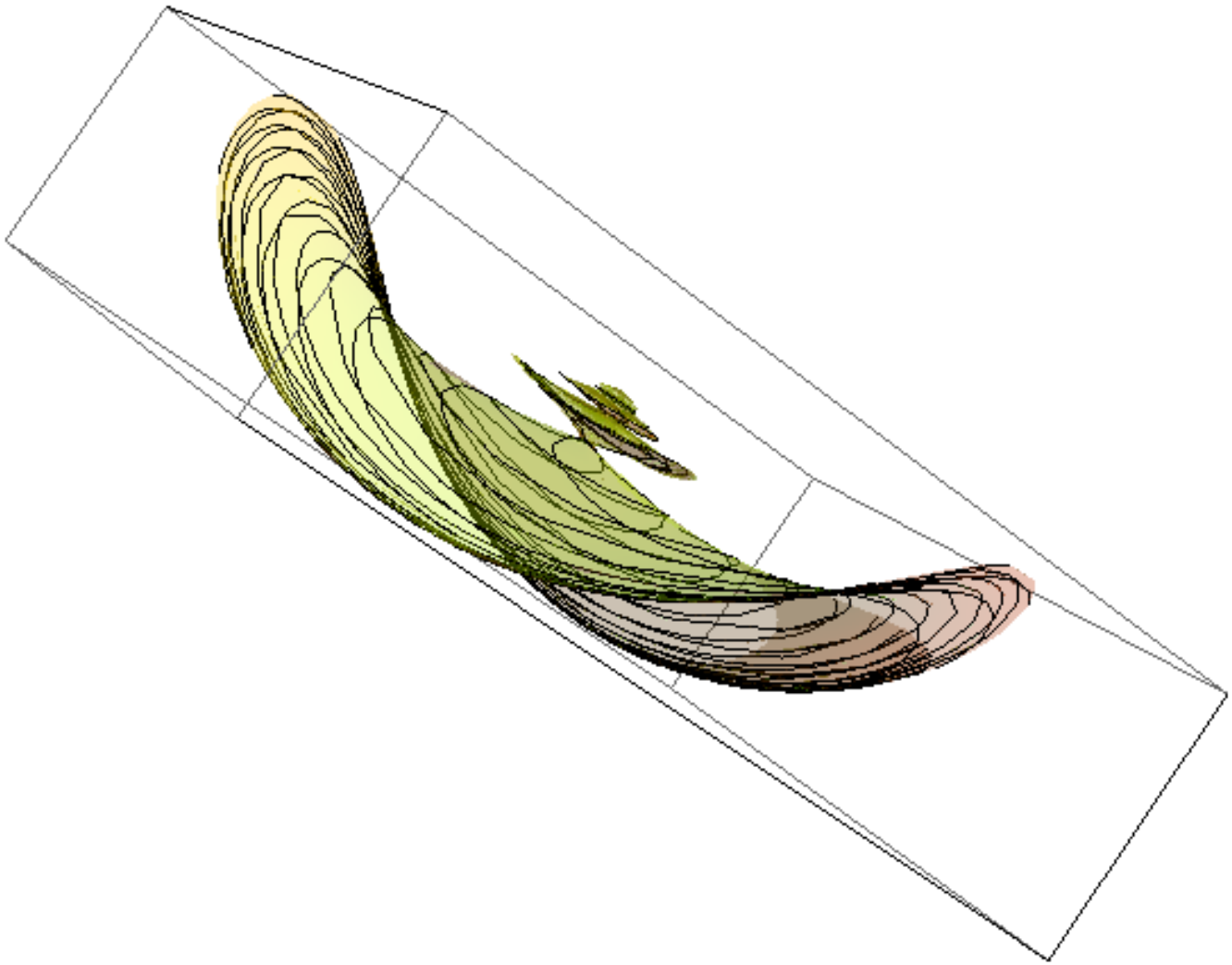

102. Exceptional level lines

In the formulas for strata C_1 and C_2, the Jacobi elliptic functions have a period $T_1(k) = 4K(k)$ for C_1 and $T_2(k) = 4kK(k)$ for C_2, where $K(k)$ is the complete integral of the first kind.

As $\varphi_t = \varphi + t$, then if $t = T(k) = R$, the formulas can be simplified.

For C_1, as $K(k) \geqslant \frac{1}{2}\pi$, there exists a solution k_R only if $t \geq 2\pi$.

103. Exceptional level lines

But for C_2 (e.g. C_2^+) there exists *always* a solution k_R of $t = R = 4kK(k)$ and then, for $k = k_R$, we get exceptional level lines:

$$\begin{cases} \theta_R = 0 \\ x_R = k_R \,\mathrm{sn}\left(\frac{\varphi}{k_R}, k_R\right)\left(\frac{R}{k_R} - \mathbb{E}\left(\frac{R}{k_R}\right)\right) \\ y_R = -\,\mathrm{dn}\left(\frac{\varphi}{k_R}, k_R\right)\left(\frac{R}{k_R} - \mathbb{E}\left(\frac{R}{k_R}\right)\right) \end{cases}$$

104. Exceptional level lines

And as $\mathrm{sn}\,(\varphi + 2K, k) = -\,\mathrm{sn}\,(\varphi, k)$ while $\mathrm{dn}\,(\varphi + 2K, k) = \mathrm{dn}\,(\varphi, k)$, the exceptional level line L_{k_R} is *degenerate* since y_R being of period only $2K$ takes twice the same value.

I made some pictures.

105. Transition between L_{k_R} and $L_{k_{c,R}}$

We have $k_{\frac{\pi}{2}} \sim 0.246139$. For $k_{c,\frac{\pi}{2}} \sim 0.2541$ neighbor of $k_{\frac{\pi}{2}} \sim 0.246139$ and solution of a more complex equation found by Sachkov, there exists another degenerate level line $L_{k_{c,\frac{\pi}{2}}}$ ("c" for critical). The geometry of the wave-front $W\left(0, \frac{\pi}{2}\right)$ between these values is particular.

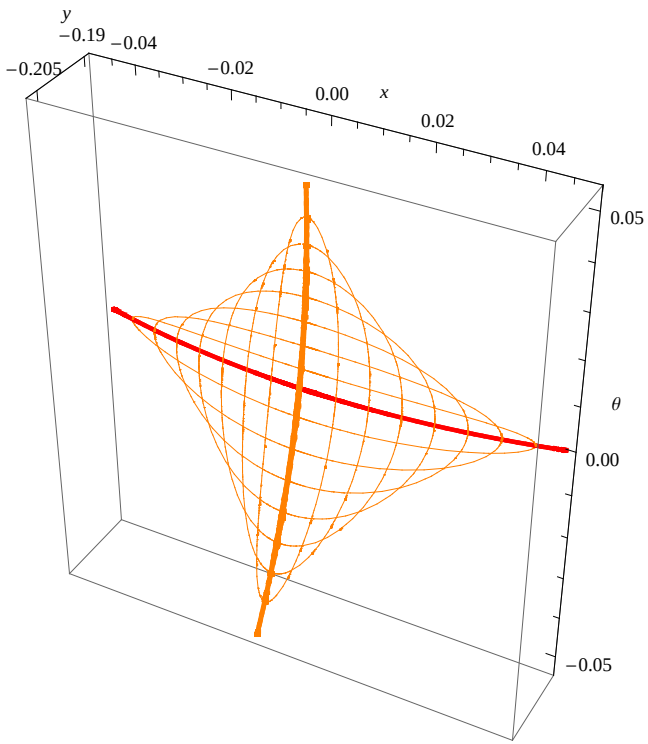

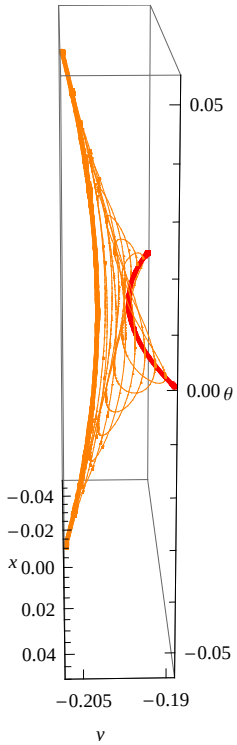

106. Intermediary "Tetrapaks"

This geometry of transition between L_{k_R} and $L_{k_{c,R}}$ unfolds the singular points on the y-axis in the Heisenberg case.

It has the shape of a "tetrapak" of which a simple model is represented in the following figure

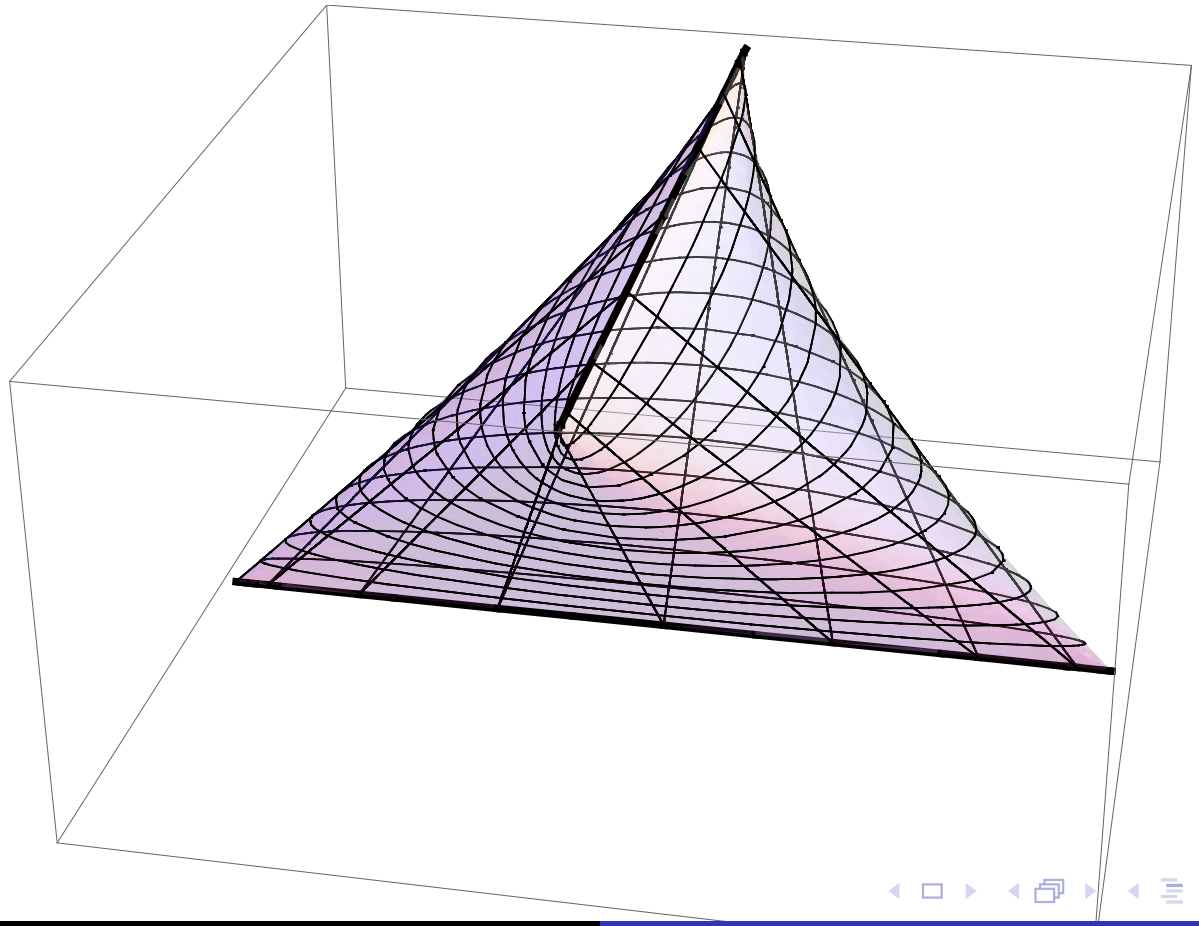

107. $W\left(0, \frac{\pi}{2}\right)$ for $k \in [0.24, 0.26]$

The following figure shows the front $W\left(0, \frac{\pi}{2}\right)$ for $k \in [0.24, 0.26]$ with the "tetrapak" transition between the degenerate level lines $k_{\frac{\pi}{2}} \sim 0.246139$ and $k_{c,\frac{\pi}{2}} \sim 0.254126$.

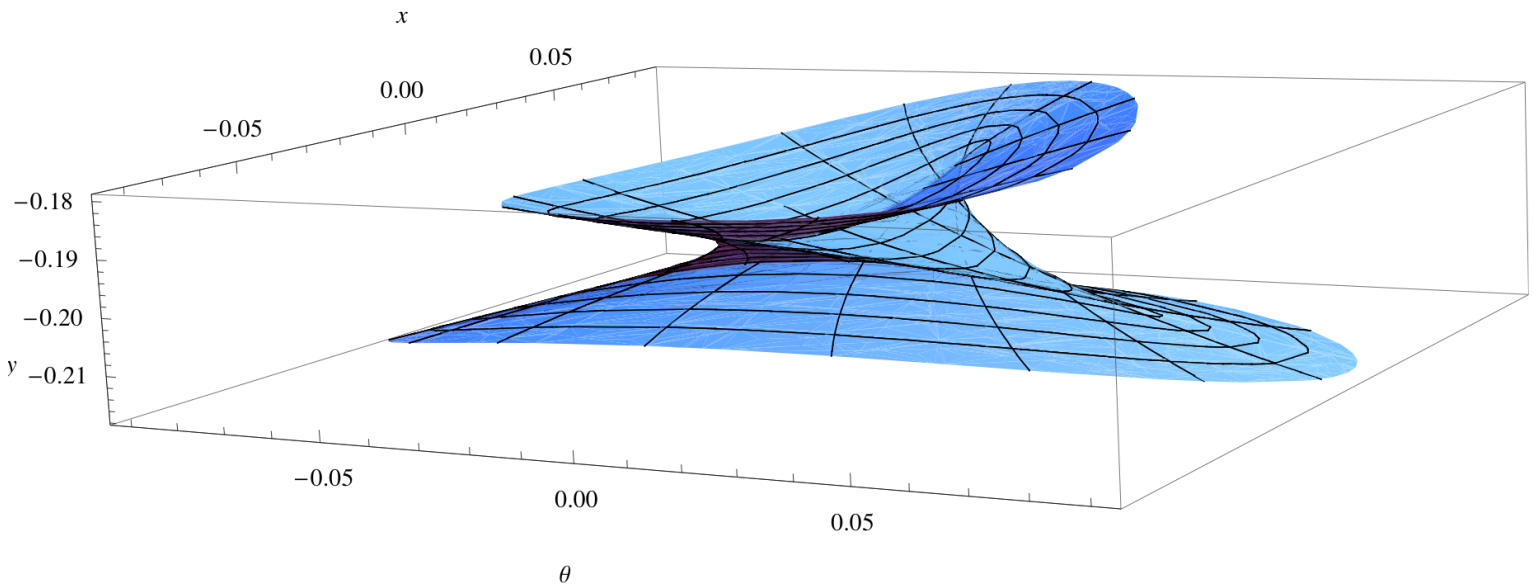

108. Maxwell strata and cut locus

The fact that the level line L_k is degenerate for the value $k_{c,R}$ is subtle. It results from technical formulas: $k_{c,R}$ is the *first zero* $p_1(k)$ (i.e. the largest) of the function

$$f(t,k) = \mathrm{cn}\left(\frac{t}{2k},k\right)\left(\mathbb{E}\left(\frac{t}{2k}\right) - \frac{t}{2k}\right) - \mathrm{dn}\left(\frac{t}{2k},k\right)\mathrm{sn}\left(\frac{t}{2k},k\right)$$

This means that we are on a Maxwell stratum and that R is the *cut-point* $t_{cut} = 2kp_1(k)$.

109. Caustic

When the radius R varies, the ends of the degenerate level lines L_{k_R} and $L_{k_{c,R}}$ run along four branches which split the y-axis of the Heisenberg case (caustic).

The figure displays the L_{k_R} (in red) and the $L_{k_{c,R}}$ (in orange) for R varying from 0 to $\frac{3\pi}{2}$ in steps of $\frac{\pi}{6}$.

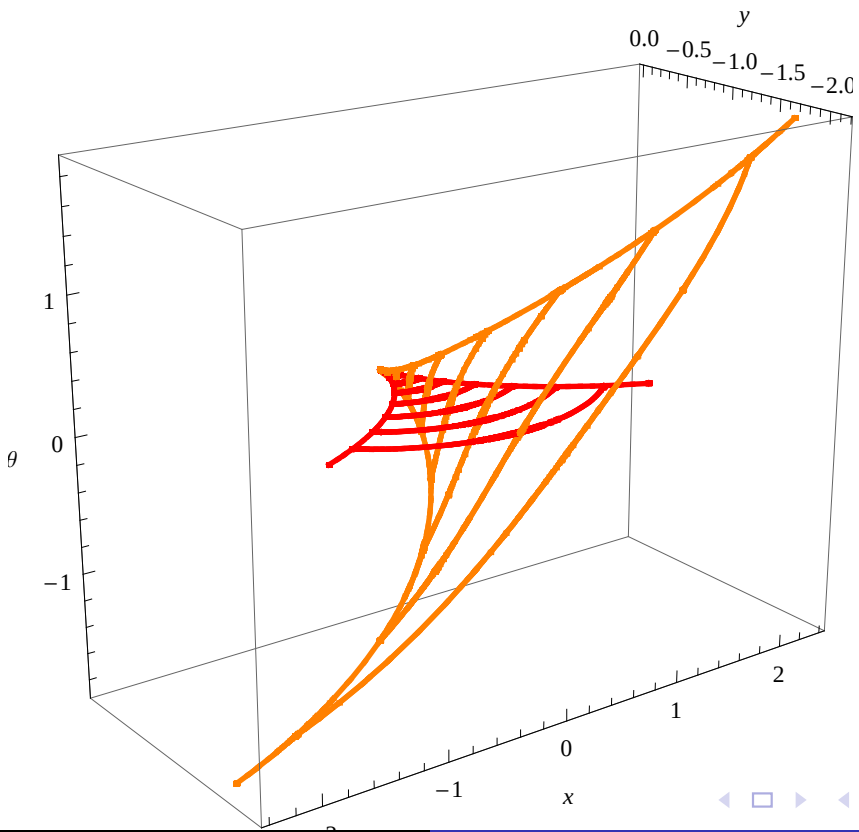

110. $SE(2)$ wave front

Next figure displays (with two viewpoints) the sphere $S\left(0, \frac{\pi}{2}\right)$ and the wavefront $W\left(0, \frac{\pi}{2}\right)$ for $k \leq 0.8$.

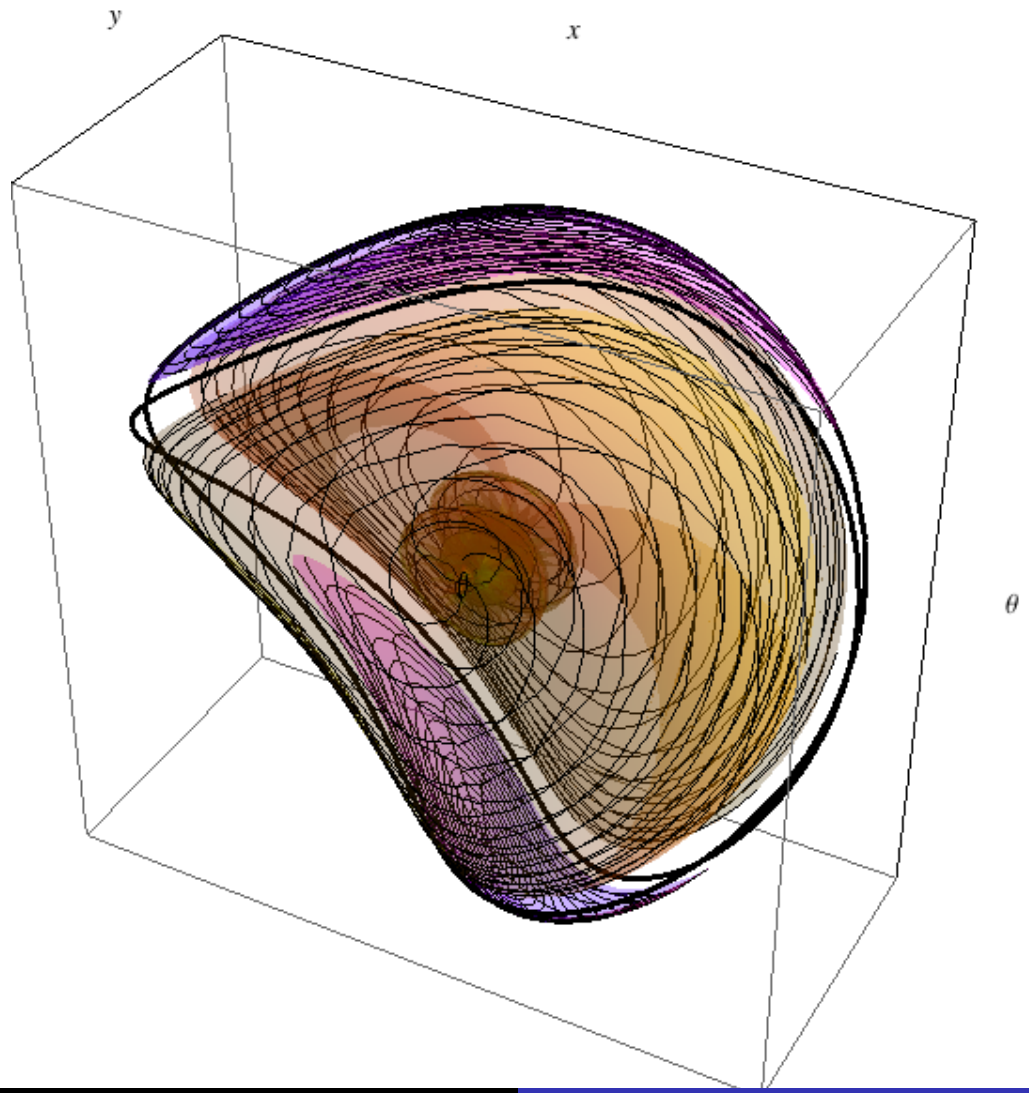

111. $SE(2)$ wave front

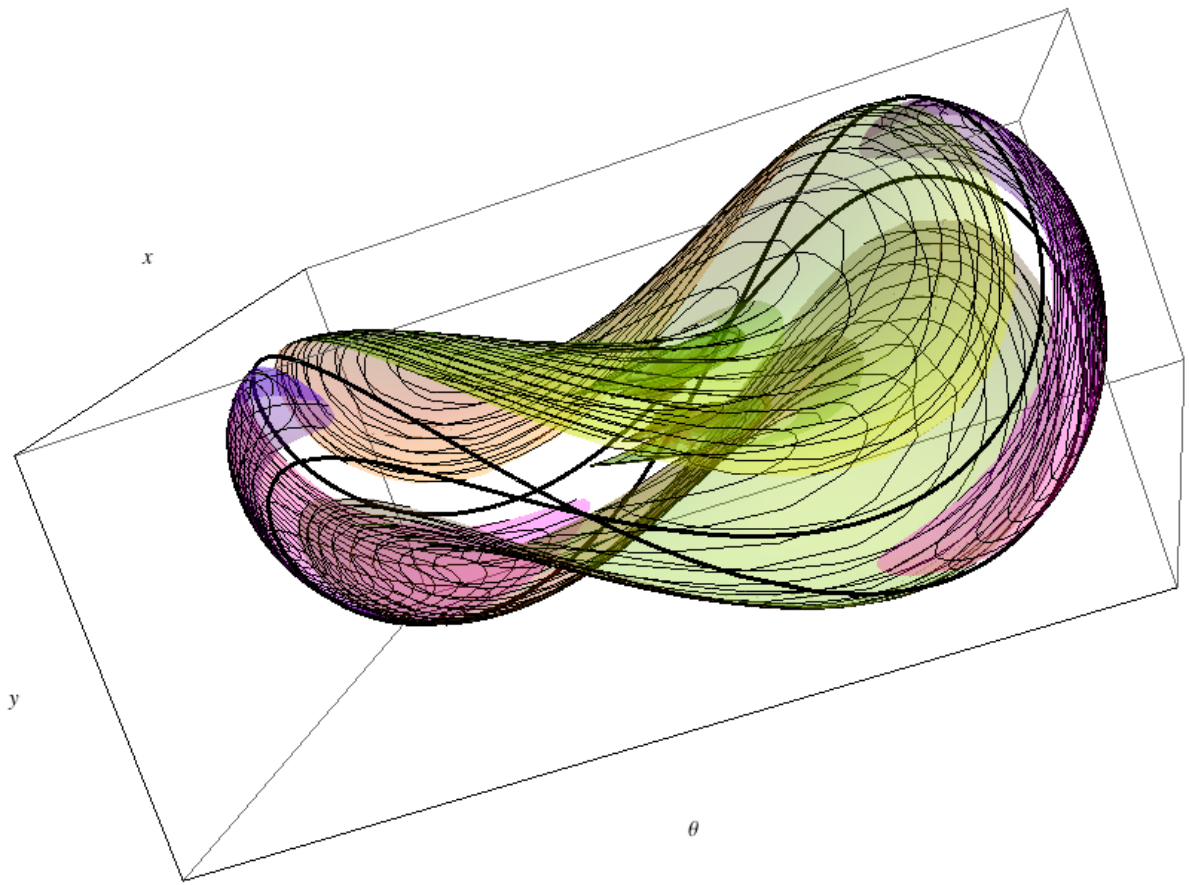

112. $W(0, R = \frac{3\pi}{2})$

As the radius R of the sphere $S(0, R)$ and of the wavefront $W(0, R)$ increases, the distortions increase.

Next figure shows four viewpoints on the image $W_{C_1^0, R=\frac{3\pi}{2}} \cup W_{C_1^{2\pi}, R=\frac{3\pi}{2}}$ of the strata C_1^0 and $C_1^{2\pi}$ at time-length $t = R = \frac{3\pi}{2}$ for $k \in [0.1, 0.999]$ as well as the image $W_{C_3, R=\frac{3\pi}{2}}$ of the four C_3 strata which bound them.

113. $W_{C_1^0, R=\frac{3\pi}{2}} \cup W_{C_1^{2\pi}, R=\frac{3\pi}{2}}$

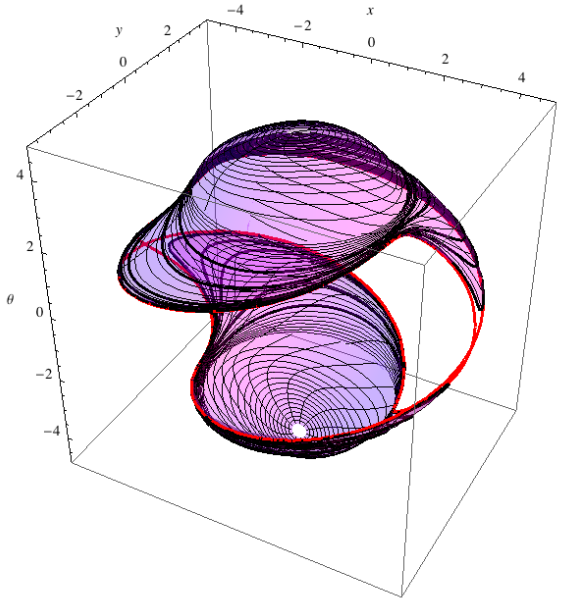

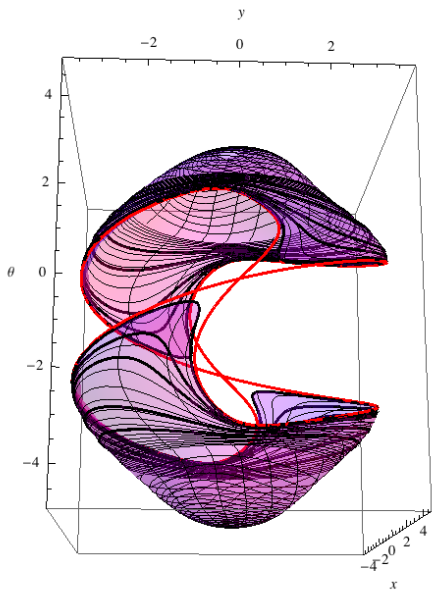

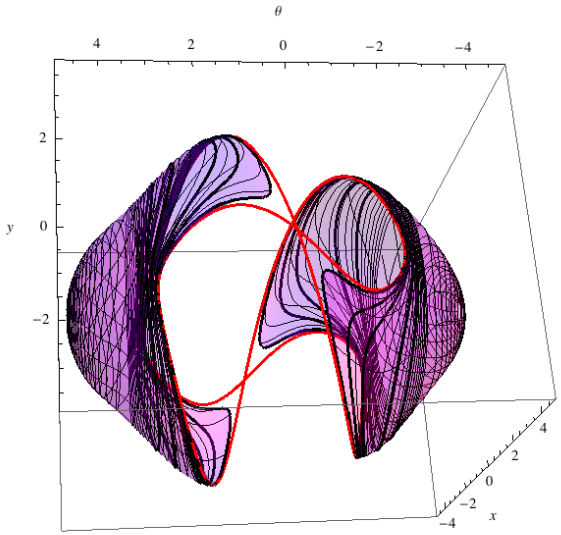

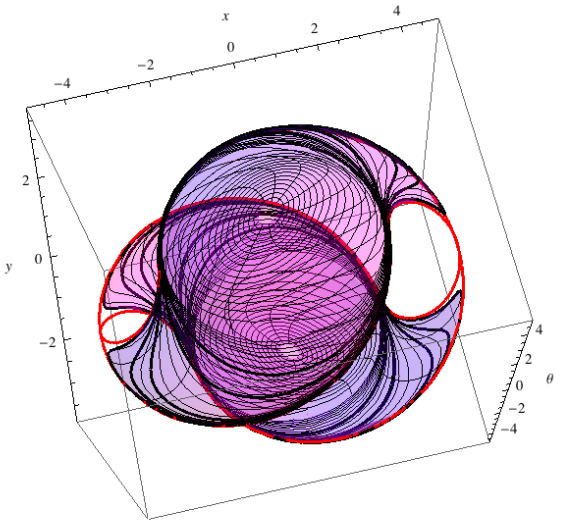

114. $W_{C_2^+,R=\frac{3\pi}{2}}$

Even more than in the case $R = \frac{\pi}{2}$, the images $W_{C_2^+,R=\frac{3\pi}{2}}$ of the strata $C_2^{\pm}$ are much more complicated with their infinity of singularities. The next figure shows some level lines L_k for $k = \text{cst}$ as well as the way in which the half profile P_0^+ of $W_{C_2^+,R=\frac{3\pi}{2}}$ (in red) intersects these level lines of level L_k when spiraling towards 0.

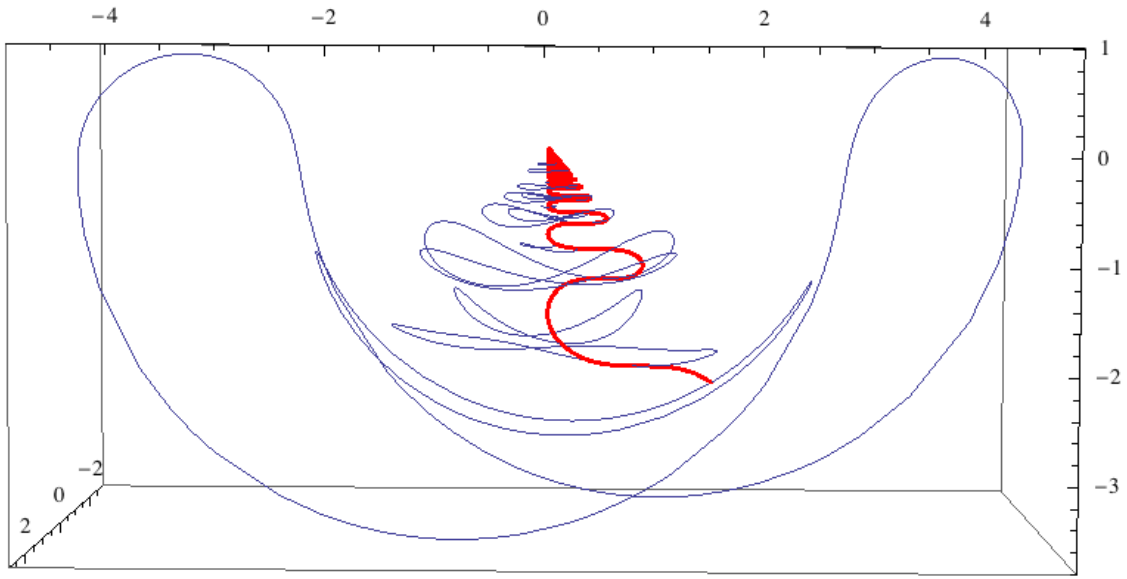

Next figure represents the image $W_{C_2^+,R=\frac{3\pi}{2}}$ of C_2^+ for $k \in [0.01, 0.999]$.

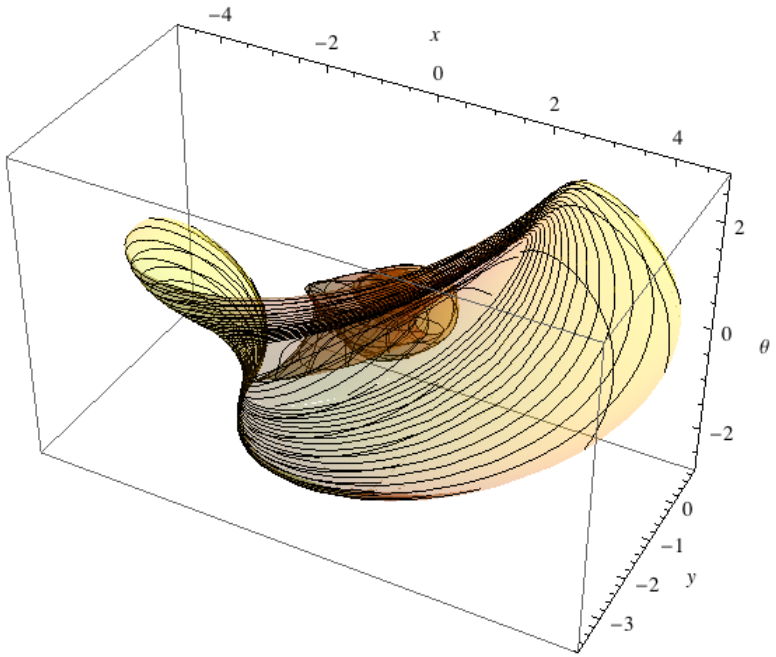

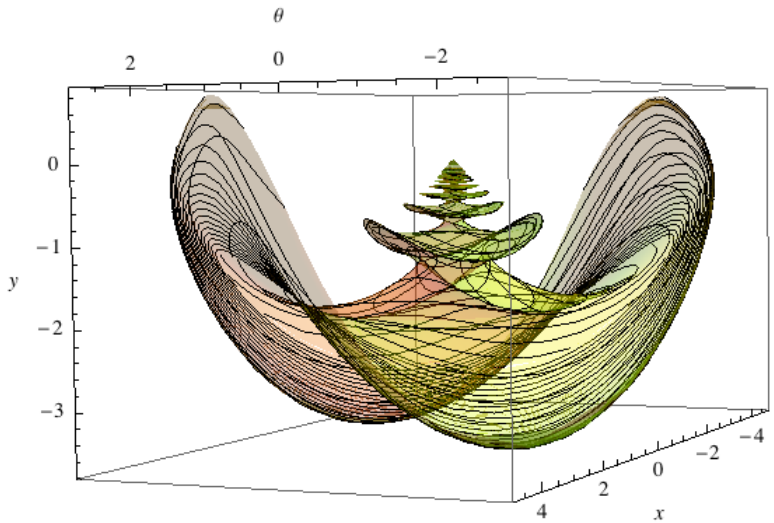

116. $W_{C_2^+,R=\frac{3\pi}{2}}$ into $W_{C_1^0,R=\frac{3\pi}{2}} \cup W_{C_1^{2\pi},R=\frac{3\pi}{2}}$

Next figure shows how $W_{C_2^+,R=\frac{3\pi}{2}}$ fits into $W_{C_1^0,R=\frac{3\pi}{2}} \cup W_{C_1^{2\pi},R=\frac{3\pi}{2}}$.

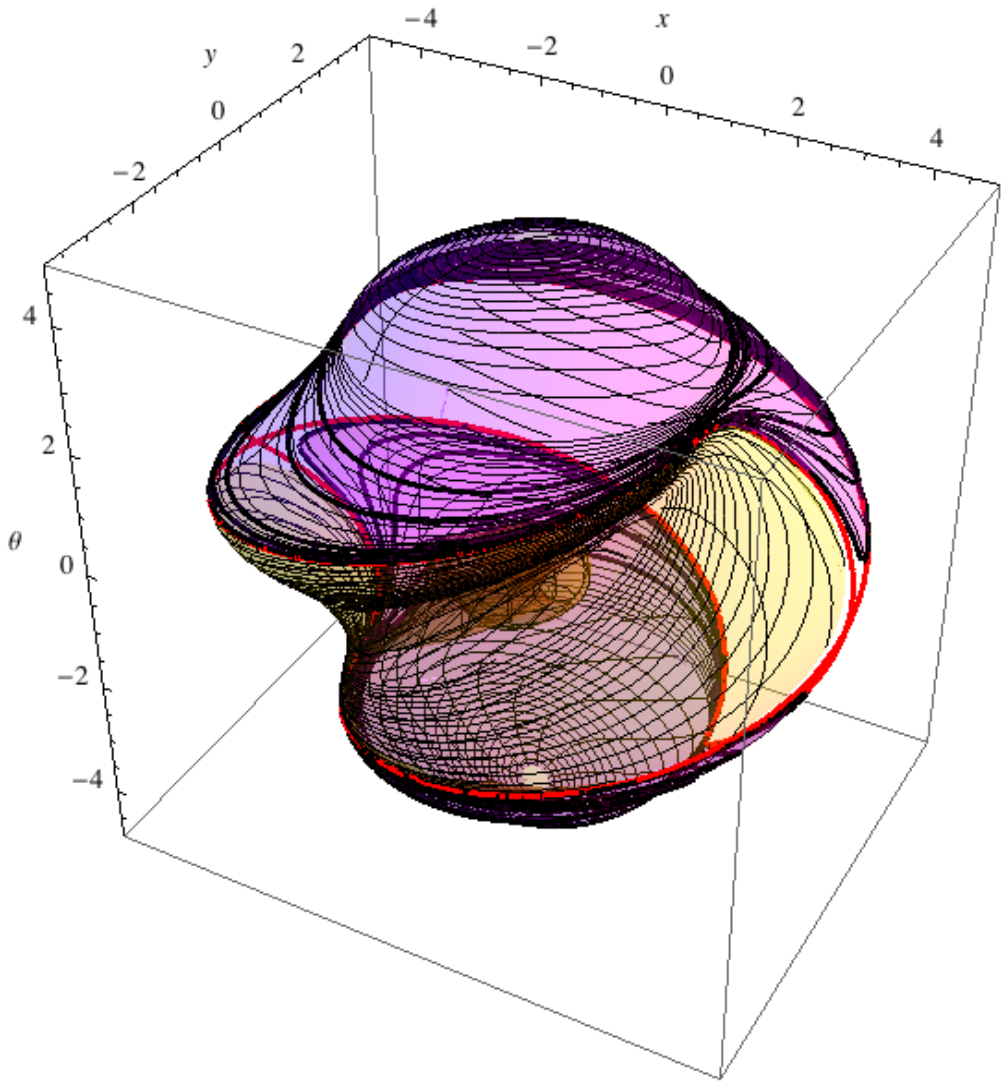

117. Complete wavefront I

Next figures show two perspectives on the complete wavefront $W\left(0, \frac{3\pi}{2}\right) = W_{C_1^0, R=\frac{3\pi}{2}} \cup W_{C_1^{2\pi}, R=\frac{3\pi}{2}} \cup W_{C_2^+, R=\frac{3\pi}{2}} \cup W_{C_2^-, R=\frac{3\pi}{2}}$.

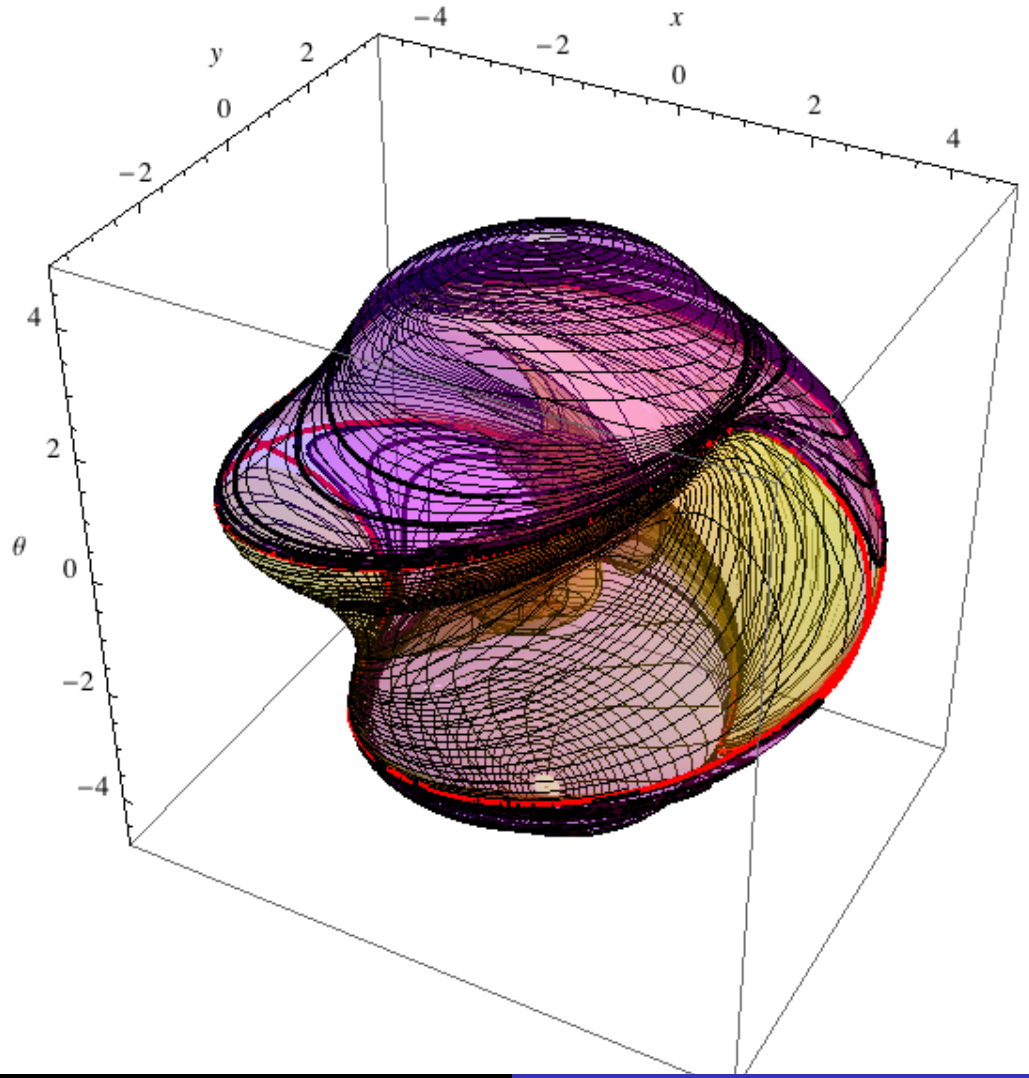

118. Complete wavefront II

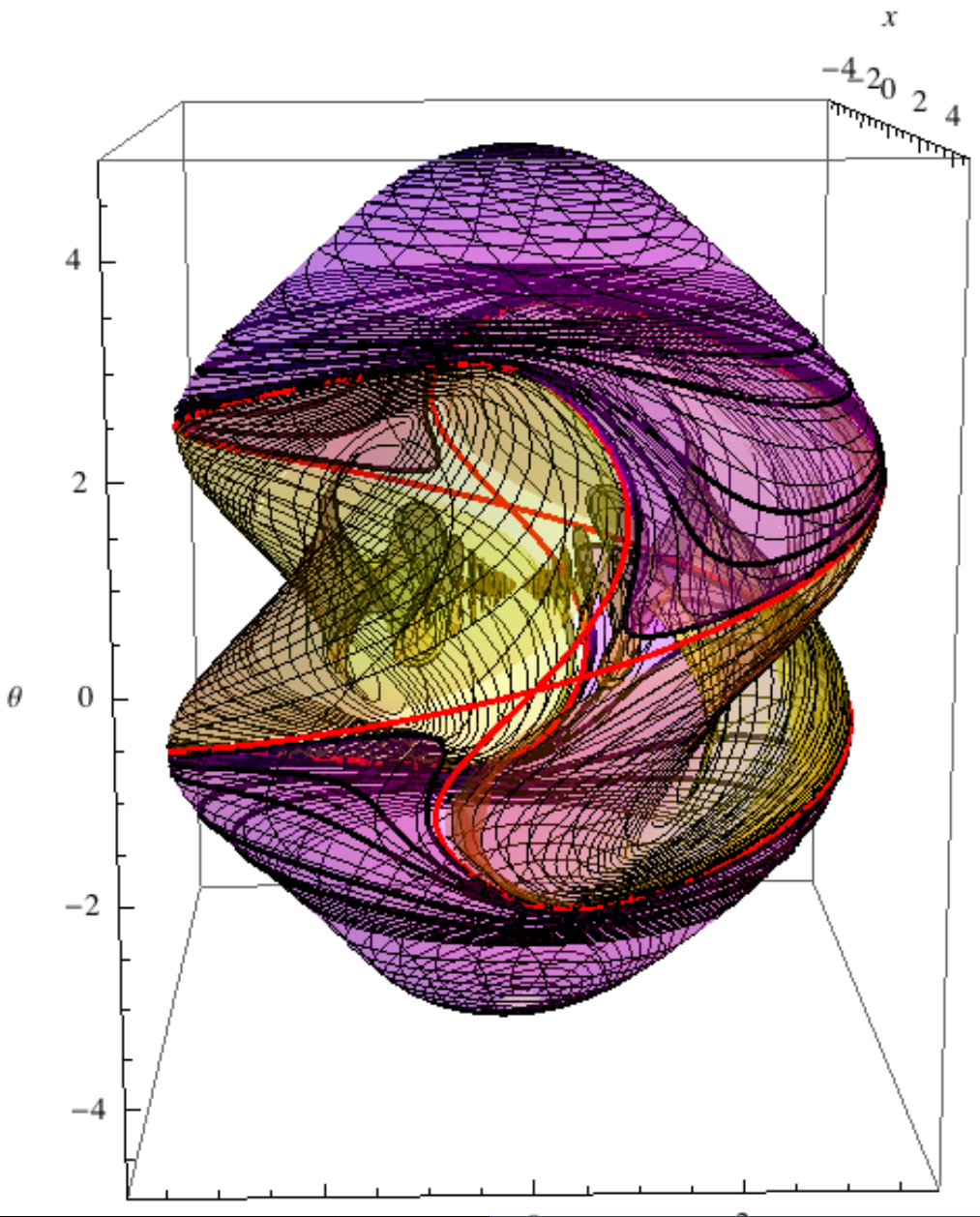

119. Wavefront modulo 2π

In the previous figures, the angle θ is not represented modulo 2π.

The following figures display $W_{C_1^0,R=\frac{3\pi}{2}} \cup W_{C_1^{2\pi},R=\frac{3\pi}{2}}$, $W_{C_3,R=\frac{3\pi}{2}}$ and the complete wavefront $W\left(0,\frac{3\pi}{2}\right)$ modulo 2π. The vertical cylinder represents the jump of θ from $-\pi$ to π.

The red curve is $W_{C_3,R=\frac{3\pi}{2}}$.

120. Wavefront modulo 2π

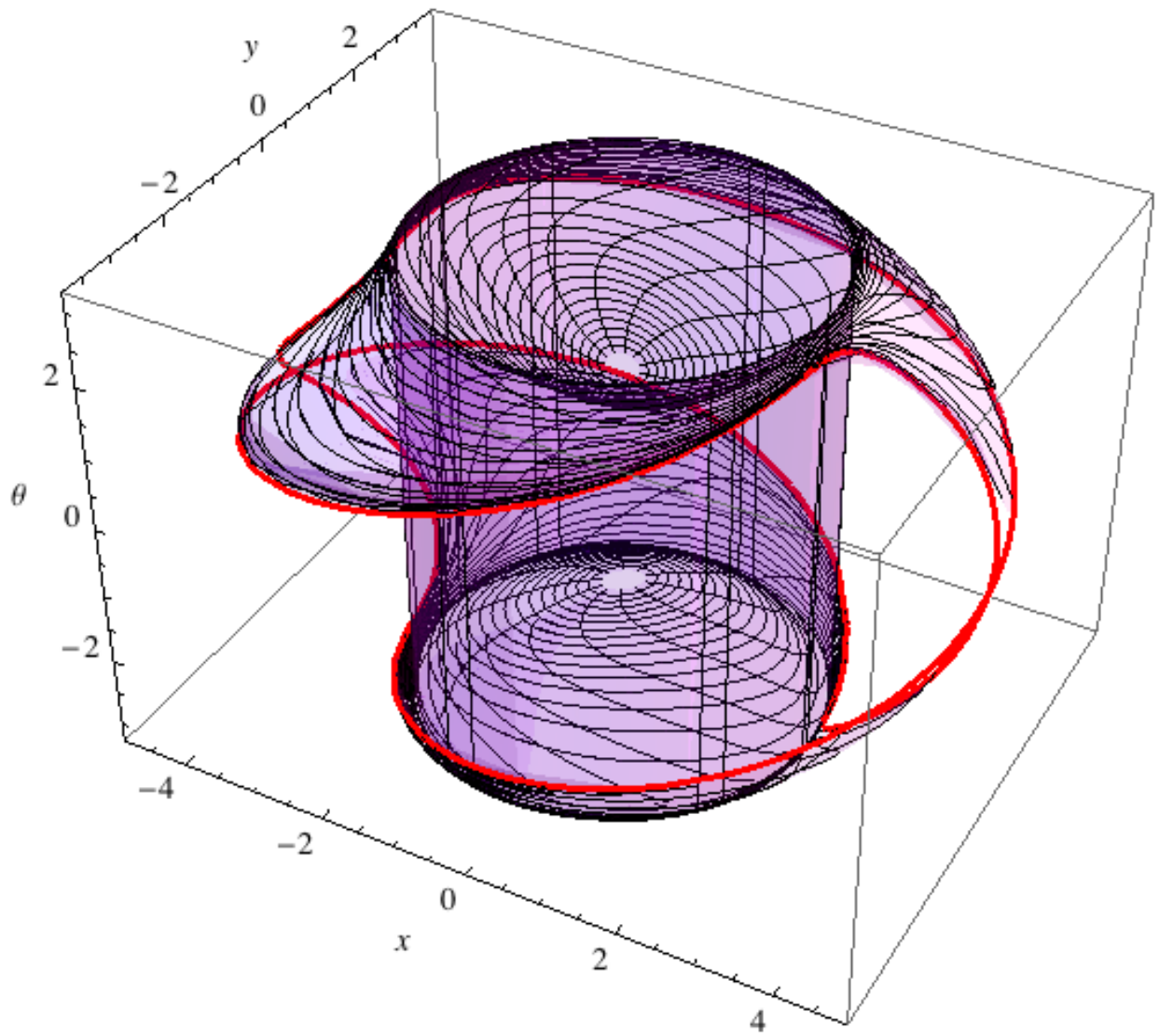

121. Wavefront modulo 2π

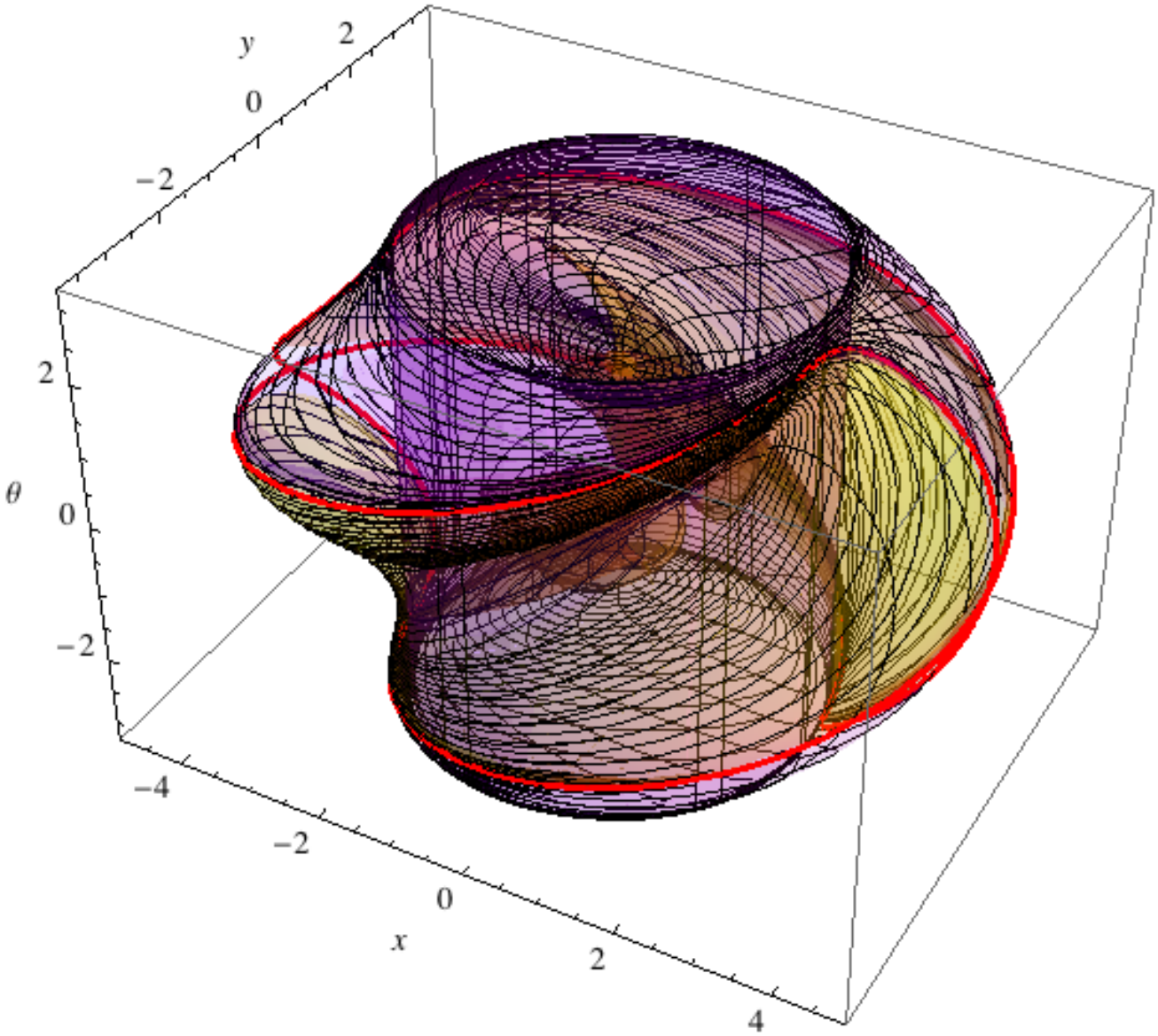

122. Toric representations for $R = \frac{3\pi}{2}$

To exemplify the toric form of the wavefront $W(0, R)$ for a radius $R > \pi$, the best is to use the toric representation and notice that $W(0, R)$ does more than one turn.

We consider therefore the torus $\mathring{\mathbb{D}}_\Lambda \times \mathbb{S}^1_{2\Lambda} = \mathbb{T}_\Lambda$ where $\mathbb{S}^1_{2\Lambda}$ is the "deferent" circle of radius 2Λ and $\mathring{\mathbb{D}}_\Lambda$ the interior of the disk in $\mathbb{R}^2$ of center 0 and radius Λ.

The new coordinates inside the torus $\mathbb{T}_\Lambda$ are
$X_{tor} = (2\Lambda + x)\cos(\theta)$, $Y_{tor} = (2\Lambda + x)\sin(\theta)$, $Z_{tor} = y$.
For $W\left(0, \frac{3\pi}{2}\right)$, we may take $\Lambda = 5$.

123. Toric representations for $R = \frac{3\pi}{2}$

The two following figures display inside the torus $\mathbb{T}_{\Lambda=5}$

1. the image $W_{C_1^0, R=\frac{3\pi}{2}}$ of the stratum C_1^0 (color magenta), and
2. the image $W_{C_1^{2\pi}, R=\frac{3\pi}{2}}$ of the stratum $C_1^{2\pi}$ (color green)

at length-time $t = R = \frac{3\pi}{2}$ for $k \in [0.01, 0.999]$.

The "horn" corresponds to lower k and the "fork" to upper k.

124. Toric $W_{C_1^0, R=\frac{3\pi}{2}}$

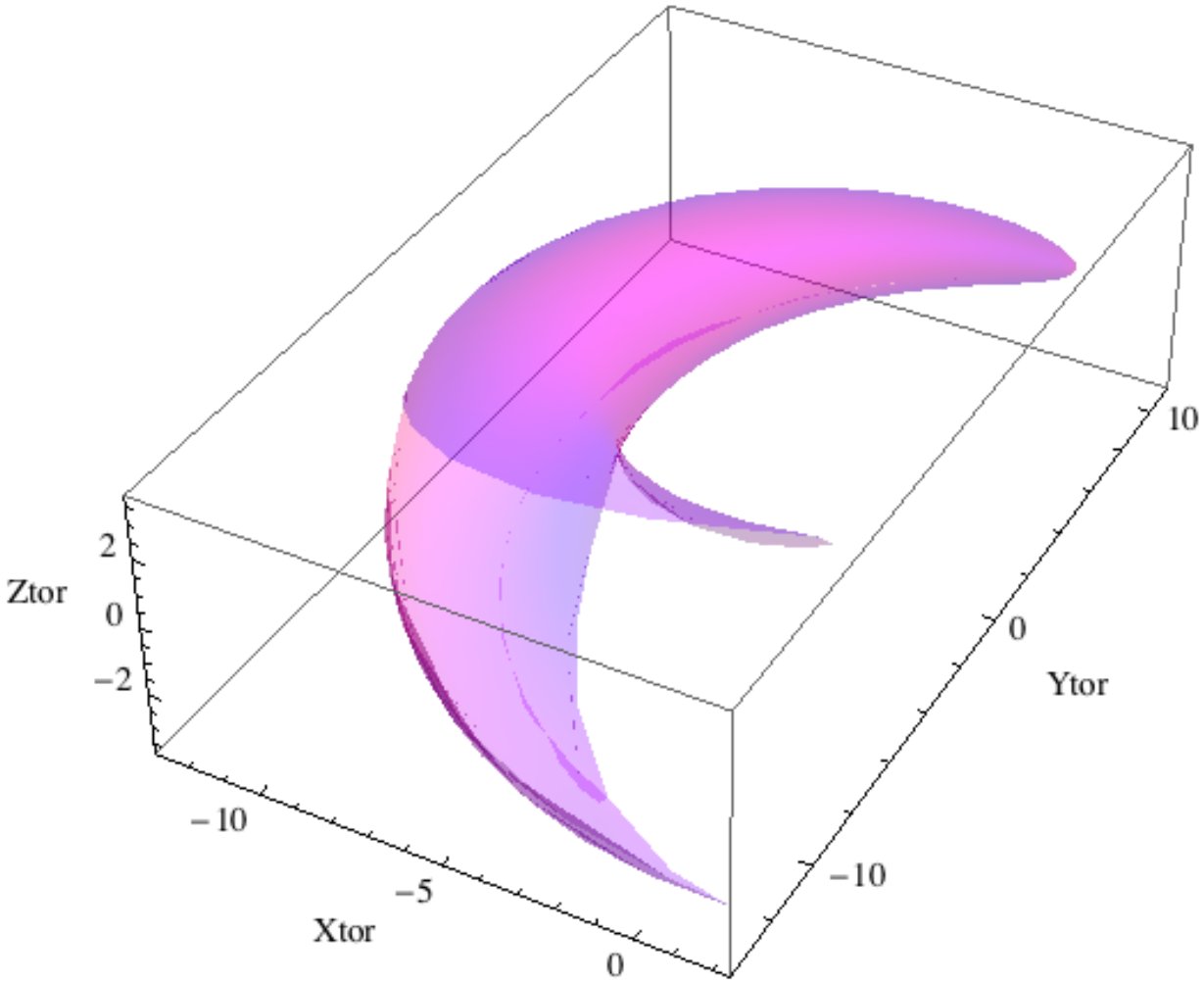

125. Toric $W_{C_1^{2\pi},R=\frac{3\pi}{2}}$

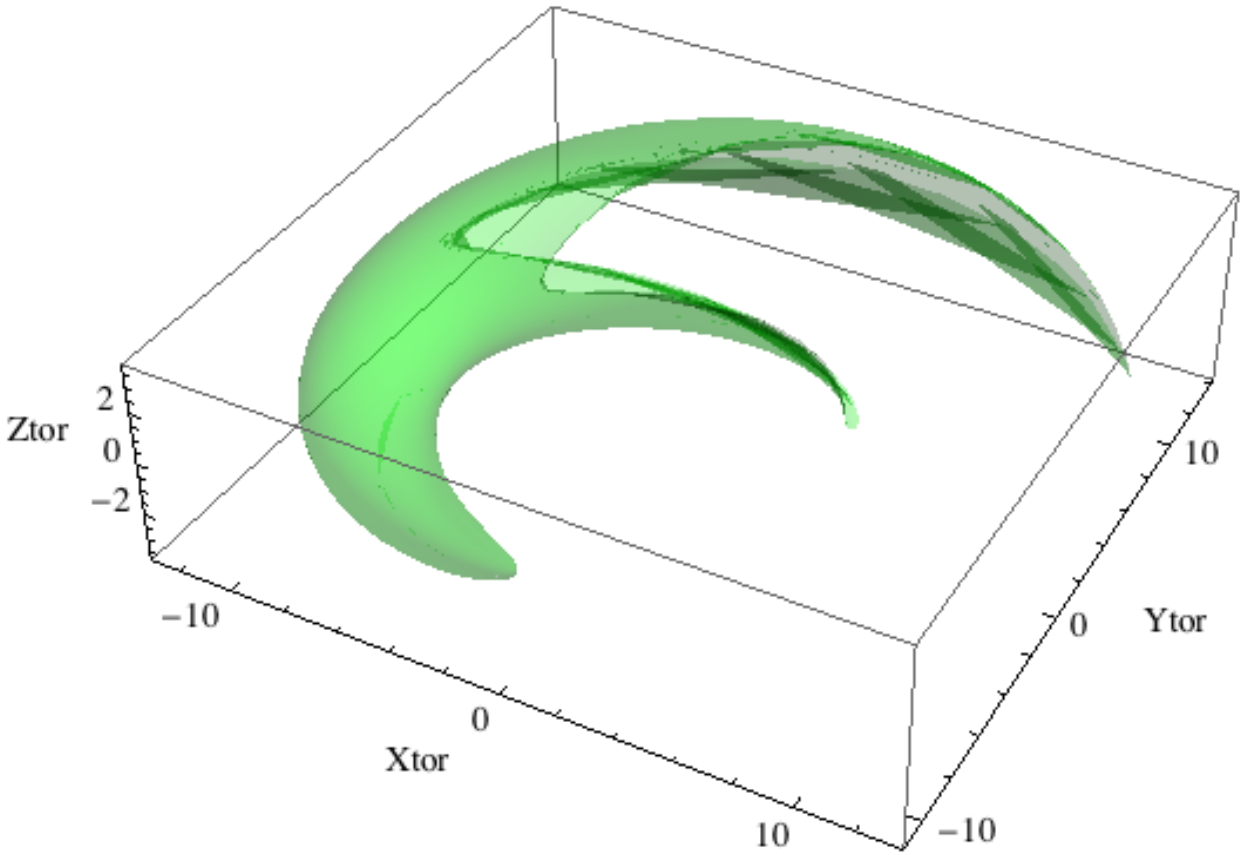

126. Intersection of $W_{C_1^0}$ and $W_{C_1^{2\pi}}$

We see in the following figure that $W_{C_1^0, R=\frac{3\pi}{2}}$ and $W_{C_1^{2\pi}, R=\frac{3\pi}{2}}$ intersect, which implies the toric form of $W\left(0, \frac{3\pi}{2}\right)$.

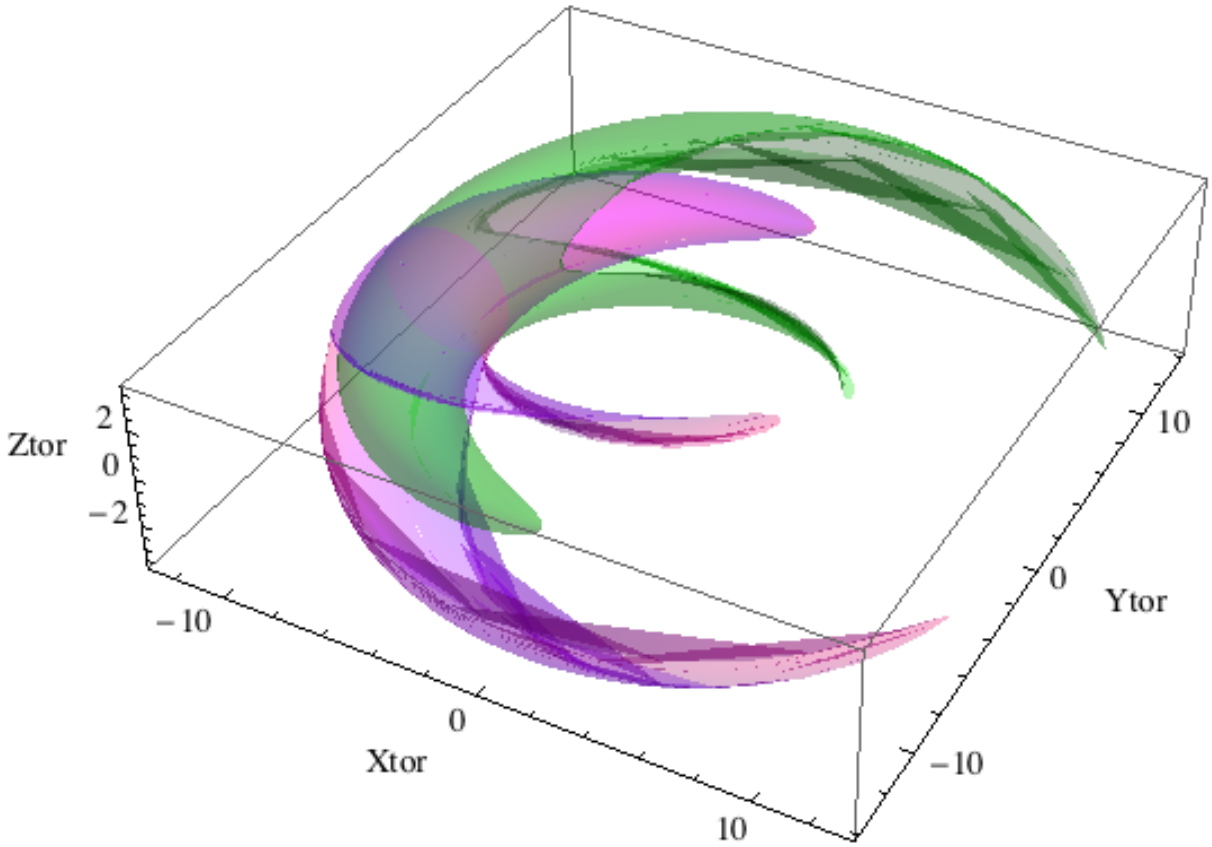

127. Toric $W_{C_2^+,R=\frac{3\pi}{2}} \cup W_{C_2^-,R=\frac{3\pi}{2}}$

For the images of the strata C_2, we get the following figure for $W_{C_2^+,R=\frac{3\pi}{2}} \cup W_{C_2^-,R=\frac{3\pi}{2}}$ for $k \in [0.5, 0.999]$ (i.e. only the first singular parts of $W\left(0, \frac{3\pi}{2}\right) - S\left(0, \frac{3\pi}{2}\right)$ are displayed).

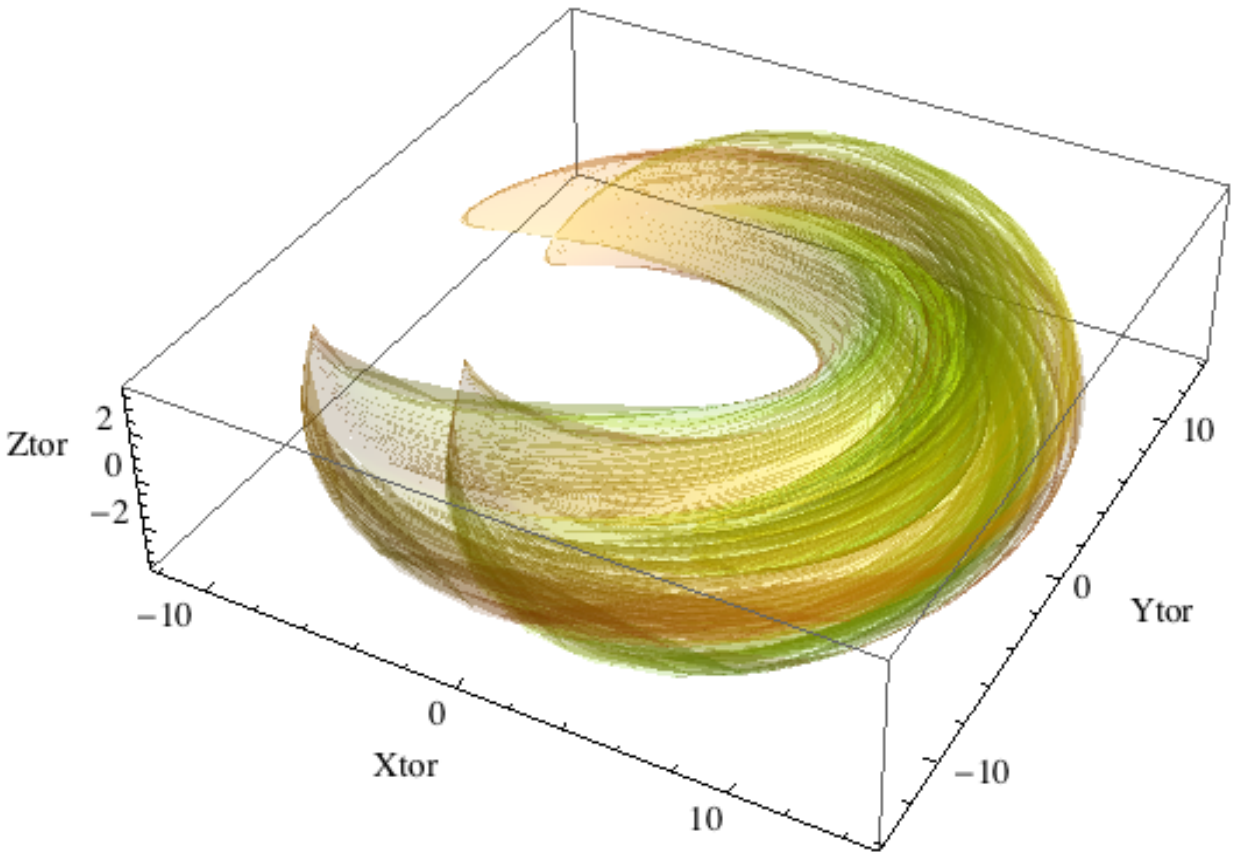

128. Toric wavefront

Finally, the following figure displays the quasi-complete wavefront $W\left(0, \frac{3\pi}{2}\right) = W_{C_1^0, R=\frac{3\pi}{2}} \cup W_{C_1^{2\pi}, R=\frac{3\pi}{2}} \cup W_{C_2^+, R=\frac{3\pi}{2}} \cup W_{C_2^-, R=\frac{3\pi}{2}}$ in the torus $\mathbb{T}_{\Lambda=5}$.

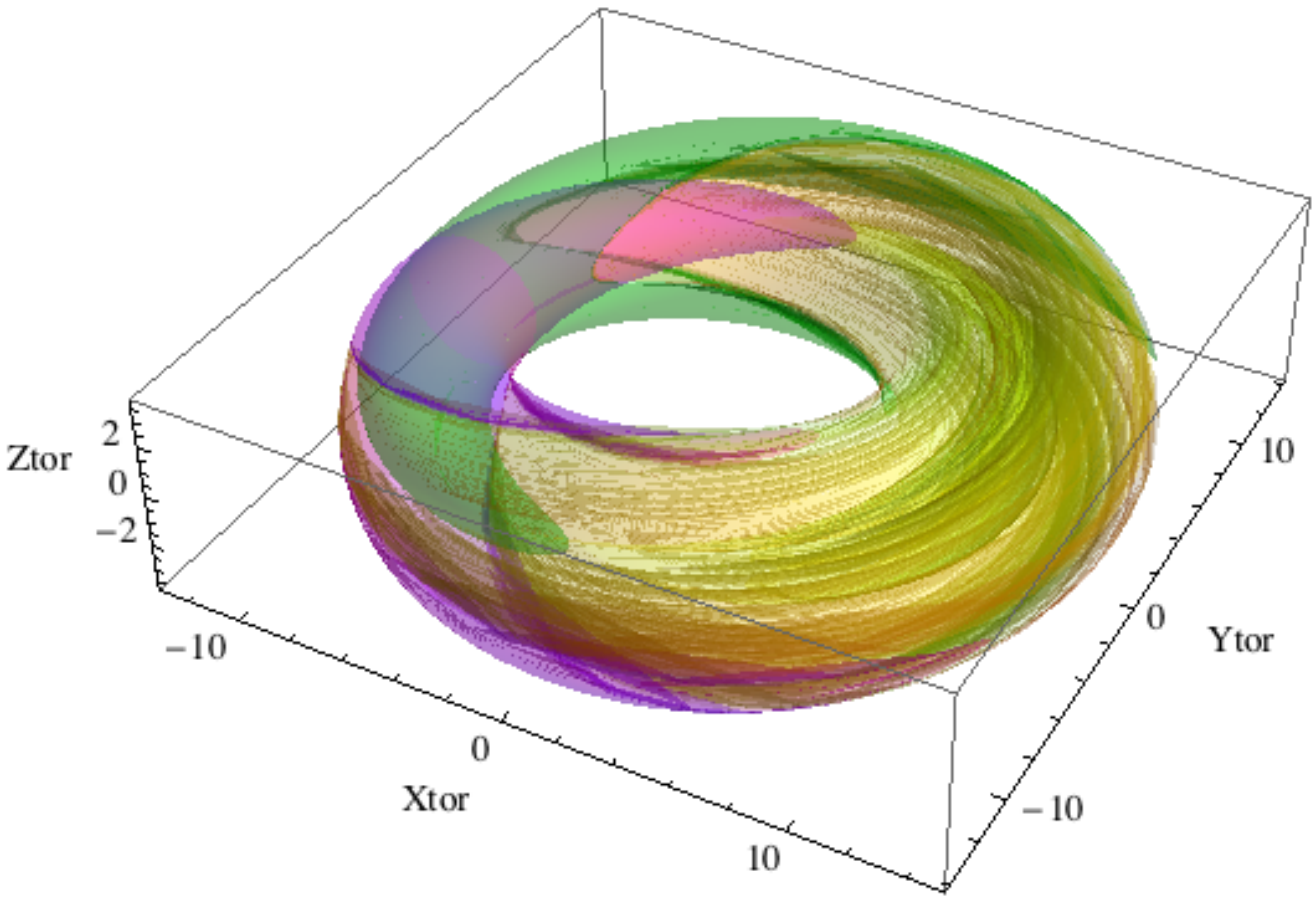

We see that the spectacular results of inpainting by means of an anisotropic diffusion along sub-Riemannian geodesics are based on a subtle geometry.

There would be a lot of other things to say about the applications of Neurogeometry in visual neuroscience. See references e.g. in some seminars of the SRGI program of Emmanuel Trélat and Davide Barilari or in the "Focus Program" of Matilde Marcolli and Doris Tsao at the Fields Institute.

But I must stop here.

Thank you for your attention.